MUNI
PŘÍRODOVĚDECKÁ
FAKULTA

MEASUREMENTS BY CUBESATS: BACKGROUND LEVELS AT LOW EARTH ORBIT, TRAPPED PARTICLE MODELS AND GAMMA-RAY TRANSIENTS

NIKOLA HUSÁRIKOVÁ

Školitel: RNDr. Jakub Řípa, Ph.D.
Ústav teoretické fyziky a astrofyziky
Přírodovědecká fakulta
Masarykova Univerzita

Brno – 2024

BIBLIOGRAFICKÝ ZÁZNAM

Autor: Nikola Husáriková
Přírodovědecká fakulta, Masarykova Univerzita
Ústav teoretické fyziky a astrofyziky

Název práce: Měření pomocí CubeSatelitů: úrovně pozadí na nízké oběžné dráze Země, modely zachycených částic a transientů gama záření

Studijný program: Fyzika

Obor: Astrofyzika

Vedoucí práce: RNDr. Jakub Řípa, Ph.D.

Akademický rok: 2023/2024

Počet stran: xiv + 72

Klíčová slova: GRBAlpha, Healpix mapa, Van Allenovy pásy, AP8/AE8, AP9/AE9, detekční algoritmus

BIBLIOGRAPHIC ENTRY

Author:	Nikola Husáriková Faculty of Science, Masaryk University Department of Theoretical Physics and Astrophysics
Title of Thesis:	Measurements by CubeSats: background levels at low Earth orbit, trapped particle models and gamma-ray transients
Degree Programme:	Physics
Field of Study:	Astrophysics
Supervisor:	RNDr. Jakub Řípa, Ph.D.
Academic Year:	2023/2024
Number of Pages:	xiv + 72
Keywords:	GRBAlpha, Healpix map, Van Allen belts AP8/AE8, AP9/AE9, trigger algorithm

ABSTRAKT

Výzkum záření zachycených částic na nízké oběžné dráze Země (LEO) je zásadní pro odhad rizik, které toto záření představuje pro vesmírné mise. Družice GRBAlpha, vybavená detektorem gama záření na své polární dráze, je schopna toto záření detekovat. V našem výzkumu porovnáváme naměřená data ze satelitu GRBAlpha (a VZLUSAT-2) s predikcemi z modelů zachycených nabitých částic AP8/AE8 a AP9/AE9 a objevujeme rozdíly mezi naměřeným a predikovaným prostorovým rozložením oblastí zachycených nabitých částic, které představují oblasti s nejvýznamnějšími toky částic v LEO. Dále používáme naměřené pozadí k ověření detekčního algoritmu a zároveň k určení jeho kritického prahového parametru. Naměřené pozadí také používáme k definování oblastí nízkého pozadí, kde detekční algoritmus funguje optimálně. Identifikace oblastí s nízkým pozadím spolu s optimální hodnotou prahového parametru detekčního algoritmu minimalizuje počet falešných spouštění, čímž ukazuje potenciál použití algoritmu v budoucích misích CubeSat.

ABSTRACT

Research on trapped particle radiation in low Earth orbit (LEO) is crucial for estimating the risks this radiation poses to space missions. Satellite GRBAlpha, equipped with a gamma-ray detector in its polar orbit, is able to detect this radiation. In our research, we compare measured data from satellite GRBAlpha (and VZLUSAT-2) with predictions from AP8/AE8 and AP9/AE9 trapped charged particle models and discover differences between the measured and predicted spatial distribution of trapped charged particle regions, which represent the areas with the most significant particle fluxes within LEO. Furthermore, we use the measured background to validate the trigger algorithm while also determining its critical threshold parameter. We also use the measured background to define regions of low background where the triggering algorithm performs optimally. The identification of areas with low background, together with the optimal value of the trigger algorithm's threshold parameter, minimizes the number of false triggers, thereby showing the potential of using the algorithm in future CubeSat missions.

MUNI
SCI

MASARYKOVA UNIVERZITA
PŘÍRODOVĚDECKÁ FAKULTA
KOTLÁŘSKÁ 2, 611 37 BRNO
IČ: 00216224
DIČ: CZ00216224

ZADÁNÍ
DIPLOMOVÉ PRÁCE

Akademický rok: 2023/2024

Ústav:	Ústav teoretické fyziky a astrofyziky
Studentka:	Bc. Nikola Husáriková
Program:	Fyzika
Specializace:	Astrofyzika

Ředitel *ústavu* PřF MU Vám ve smyslu Studijního a zkušebního řádu MU určuje diplomovou práci s názvem:

Název práce:	Measurements by CubeSats: background levels at low Earth orbit, trapped particle models and gamma-ray transients
Název práce anglicky:	Measurements by CubeSats: background levels at low Earth orbit, trapped particle models and gamma-ray transients
Jazyk závěrečné práce:	angličtina

Oficiální zadání:
The GRBAlpha nanosatellite, a 1U sized CubeSat, was launched in March 2021 into low Earth Sun-synchronous orbit, and it carries on board a gamma-ray detector capable of detecting gamma-ray transient events. The detector consists of 75 mm x 75 mm x 5 mm CsI(Tl) scintillator, read out by a dual-channel multi-pixel photon counter (MPPC) setup. One of the goal of GRBAlpha is to measure the levels of the background at low Earth orbit. The nanosatellite has proven its functionality and it has recorded plenty of valuable measurements which should be analysed in detail. One of the advantage of the innovative detector on board of GRBAlpha is that it can operate also inside the Van Allen radiation belts (polar regions and the South Atlantic Anomaly) where the particle flux is several orders of magnitude higher than in the quiescent low latitude regions. Beyond all expectations the satellite has also detected several gamma-ray bursts.

The goal of this project is to compare the in situ measurements of the background levels with the existing models of the trapped charged particle fluxes, such as NASA's legacy AE-8/AP-8 or newer AE-9/AP-9 models. These models are available either through the AFRL's software or via the ESA's WWW interface SPENVIS. Study of the distribution of the background levels, the temporal variability and possibly also anisotropy of the trapped charged particle flux will be highly beneficial for the planned low Earth satellite missions.

The accurate understanding of the recorded background is important for the efficient search of gamma-ray transients with the astrophysical origin such as gamma-ray bursts, soft gamma repeaters and solar flares. The next goal of this project is thus to search for these transient events in the observed light curves.

Another nanosatellite called VZLUSAT-2 is scheduled to be launched in Dec 2021 and it is anticipated that it will also bring plenty of valuable measurements which can be also analysed within this project.

Vedoucí práce:	RNDr. Jakub Řípa, Ph.D.
Konzultant:	Mgr. Filip Hroch, Ph.D. Mgr. Filip Münz, PhD. Dr. Martin Topinka, PhD. Jean-Paul Bernhard Riffald Souza Breuer
Datum zadání práce:	6. 11. 2021
V Brně dne:	16. 11. 2023

Bc. Nikola Husáriková, 7. 1. 2022
RNDr. Jakub Řípa, Ph.D., 8. 1. 2022
Mgr. Dušan Hemzal, Ph.D., 25. 1. 2022

ACKNOWLEDGEMENTS

First and foremost, I would like to thank my supervisor, Jakub, for guiding me throughout this project, providing me with numerous ideas and advice, and keeping me motivated. Furthermore, I thank everyone involved in the GRBAlpha mission from development to operation, thanks to which I was able to work on this topic, mainly to thank András Pál. Special thanks go to my father, my brother Martin and my partner Adam for their unwavering support during my studies and all the motivation, especially in the final stages of processing this work.

DECLARATION

Hereby I declare that I have prepared my Master's thesis independently under the guidance of the supervisor with the use of cited works.

Brno, 2024

Nikola Husáriková

CONTENTS

INTRODUCTION

In the Low Earth Orbit (LEO) region, CubeSats and other satellites equipped with gamma and charged particle detectors detect radiation containing different components, each contributing to the complex radiation environment. These components include the cosmic X-ray background (CXB), secondary X-rays and gamma rays originating from interactions in the Earth's atmosphere, trapped particle radiation, cosmic charged particles, and secondary particles generated in the Earth's atmosphere, radiation from our galaxy, the Sun radiation and internal background radiation resulting from the nuclear activation of materials. Among these various types of radiation in LEO, the trapped particle radiation stands out and contributes the most to the background radiation. This radiation forms the Van Allen belts and the South Atlantic Anomaly (SAA), regions that pose a risk to satellite missions.

In our work, we concentrate on trapped particles radiation in LEO, comparing trapped radiation models (such as AE8, AP8, AE9, and AP9) and measurements obtained by CubeSats GRBAlpha and VZLUSAT-2. With our analysis, we wanted to better understand the spatial distribution of these regions and thus expand our knowledge of the LEO radiation environment, which may be important for future space missions.

In the second part of the thesis, we looked at the triggering algorithm designed to identify transients. The goals of this part were to minimize the appearance of false triggers and, at the same time, ensure the highest possible number of detections of actual transients. In addition, we used the spatial distribution of the false triggers caused by background fluctuations identified by our algorithm. Areas where the trigger algorithm found a large number of false detections correspond to areas with increased background levels. By identifying these areas, future CubeSat missions can use this trigger algorithm and selectively turn off measurements in these areas to limit the number of false triggers.

The thesis consists of the following parts. In the theoretical part, we described the trapped particle radiation in the Earth's magnetic field and described the models of trapped particles AE8, AP8, AE9, and AP9. In the methodology, we further describe the GRBAlpha and VZLUSAT-2 satellites from which we obtained our data. Additionally, in this section, we describe modelling the trapped particle background for both satellites. We also provide a brief description of the trigger algorithm. In the last results and discussion section, we begin with the comparison of measured data with modelled data. At the end of this section, we evaluate the effectiveness of the triggering algorithm in minimizing false triggers.

Part I

THEORY

1

THE EARTH'S TRAPPED PARTICLE RADIATION ENVIRONMENT

The discovery in 1958 that the Earth's magnetic field contains bands of charged particles revolutionized our understanding of the Earth's magnetosphere. This environment also contains an interesting area where bands of charged particles come closest to the Earth's surface – the so-called South Atlantic Anomaly and presents a challenge and potential harm for spacecraft and people in space. To understand the behaviour of these trapped particles and to help plan other space missions, scientists have developed trapped charged particle models such as AP8, AE8, AP9 and AE9, which help predict radiation risks in space.

1.1 TRAPPED PARTICLE RADIATION

Charged particle motion is given by a Lorentz force defined as:

$$\vec{F} = q(\vec{E} + \vec{v} \times \vec{B}), \tag{1.1}$$

where q is its charge, $\vec{v}$ is its velocity vector, and $\vec{E}$ and $\vec{B}$ are vectors of electric and magnetic fields. The force acting on a charged particle is perpendicular to its velocity vector and magnetic field vector. This causes the particle to move in a circle around the magnetic field line. The radius r_g of this circle is called the gyration radius or Larmor radius. It can be determined from the equality of Lorentz force and centripetal force:

$$\begin{aligned} \frac{mv_\perp^2}{r_g} &= |q|(v_\perp B) \\ r_g &= \frac{mv_\perp}{|q|B}. \end{aligned} \tag{1.2}$$

In combination with the particle movement along the magnetic field lines, we get overall spiral motion along field lines.

When studying the motion of charged particles in Earth's inhomogeneous magnetic field, it cannot be described only with this gyromotion. Earth's magnetic field changes slowly compared to charged particles' characteristic movements. In such a field, the magnetic moment is constant and it is proportional to the gyration radius and the velocity component perpendicular to the magnetic field line (Siegl, 2009):

$$\mu \propto v_\perp r_g. \tag{1.3}$$

If the magnetic field converges, the particle feels a small force along the field line direction, increasing towards the region of converging field lines. With increasing force,

the gyration radius decreases and tangential velocity increases. However, the increase of $v_\perp$ is at the expanse of the velocity component parallel to the magnetic field line $v_\parallel$ because the total kinetic energy stays constant (Siegl, 2009):

$$\frac{1}{2}m(v_\perp^2 + v_\parallel^2) = const. \tag{1.4}$$

The point where $v_\parallel$ equals to zero is called the mirroring point. At this mirroring point, the particle feels a force in the direction away from a larger magnetic field, and it spirals back along the field line until it reaches the opposite mirroring point. This leads to bouncing motion between two mirroring points, so the particle is trapped on a specific field line (Jun and Garrett, 2005).

As a result of the force acting along magnetic field lines, the particles also undergo a slow drift around the Earth. Positively charged particles drift westward and negatively eastward (Martinez, 2011).

When combining all these motions of charged particles, they form doughnut-shaped Van Allen Belts, as shown in Figure 1.1. The population of these particles consists mainly of trapped protons and electrons, and their distribution in the Earth's magnetic field is shown in the 1.2. Van Allen belts are named after their discoverer and were first detected by the Geiger counter onboard Explorer 1, launched in 1958 (Van Allen et al., 1958). The difference in the type and energy of these particles led to the formation of two belts, an outer belt and an inner belt with its South Atlantic Anomaly (SAA) part. The appearance of these areas in the observed light curve when the GRBAlpha satellite passes through them is shown in Figure 1.3.

1.1.1 *Outer Van Allen Belt*

The outer Van Allen Belt extends from approximately 3 to 10 Earth radii $R_\oplus$, although in the polar regions where the field lines converge, it extends to a height of several hundred kilometres above the surface, so it is detectable on Low Earth Orbits (LEOs). There are mainly mildly to highly relativistic electrons with energies from 100 keV to 10 MeV. Additionally, high-energy protons can reach the belts through Solar Energetic Particle (SEP) events. However, these events are very short-lived because the large gyroscopic radii of high-energy protons prevent stable confinement in this region (Baker et al., 2017). The outer Van Allen belt is highly variable both in time and space with the primary reason being the speed of the solar wind (Baker et al., 1979).

1.1.2 *Inner Van Allen Belt*

The inner Van Allen belt is located closer to the Earth's surface, reaches an equatorial altitude of about 10,000 kilometres, and is dominated by high-energy protons (Baker

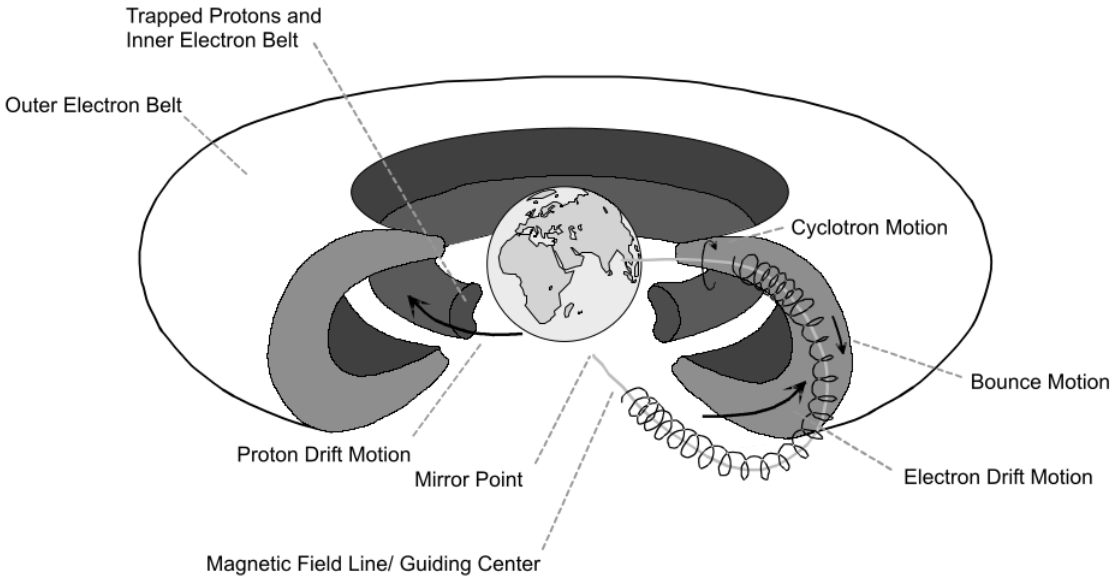

Figure 1.1: The gyro-motion, drift-motion and bounce-motion of charged particles trapped in the Earth's magnetic field forming doughnut-shaped Van Allen Belts. Figures from Motions, 2024.

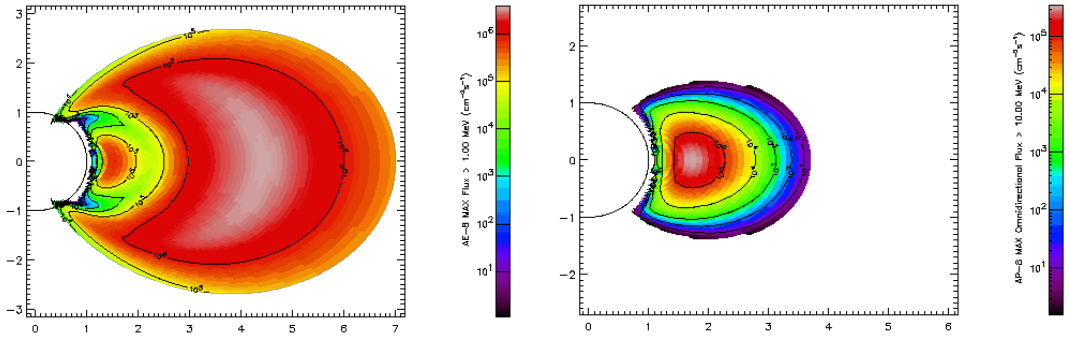

Figure 1.2: Distribution of geomagnetically trapped electrons and protons surrounding the Earth. Right: AP-8 MAX integral proton flux map exceeding 10 MeV. Left: AE-8 MAX integral electron flux map exceeding 1 MeV. A semicircle indicates the Earth's surface, with distances expressed in Earth radii. Figures from SPENVIS, 2018.

et al., 2017). These protons come primarily from the β-decay of free neutrons produced when Galactic Cosmic Rays (GCRs) interact with molecules of the Earth's atmosphere, the so-called Cosmic Ray Albedo Neutron Decay (CRAND). These protons are mainly in the energy range from 0.1 to hundreds of MeV (Siegl, 2009). They show stability at a geocentric radial distance of about 1.5 $R_\oplus$ with energies ranging from about 10 to 100 MeV (Baker et al., 2017). In the inner Van Allen belt are also electrons with low and medium energy (Fennell et al., 2015, Li et al., 2015) and ultrarelativistic electrons exceeding the energy of 2.5 MeV. Furthermore, solar energetic particles (Baker, 2002,

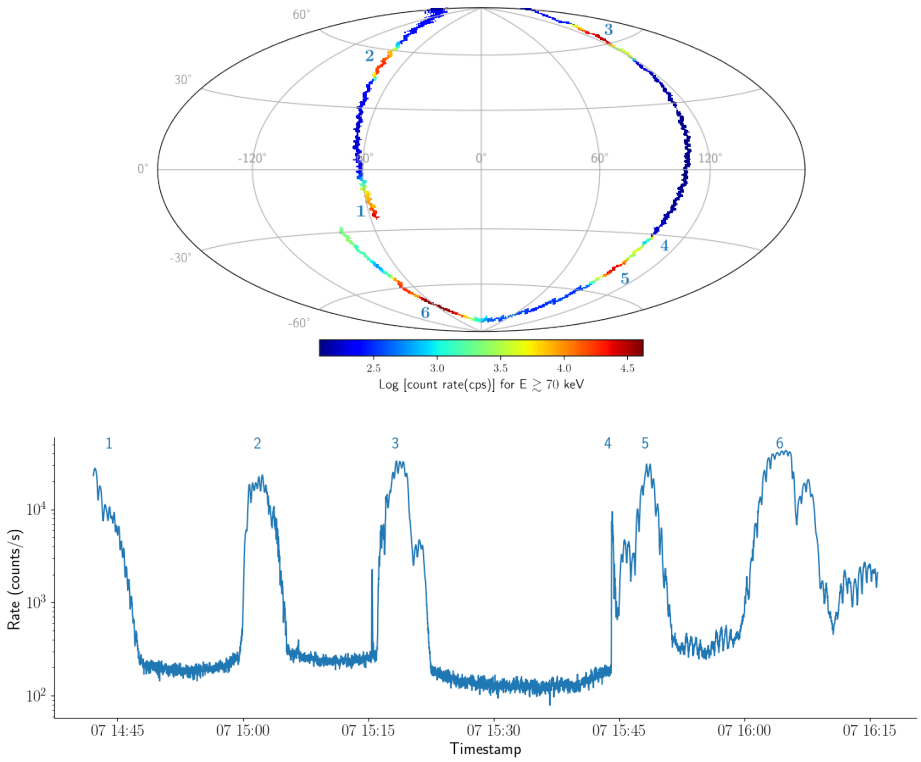

Figure 1.3: *Top*: View of one complete orbit of the GRBAlpha satellite on a map related to the detection of GRB 230307A. *Bottom*: Corresponding light curve. GRBAlpha transitions with high background areas are marked by individual numbers: in the top image by blue coloured numbers and in the bottom image above the peaks. 1) Satellite leaves SAA. 2) For the first time, it passes through the northern hemisphere's polar belt. 3) The polar belt in the northern hemisphere is traversed for the second time. 4) Detection of GRB 230307A. 5) It passes through the polar belt in the southern hemisphere for the first time. 6) It passes through the southern hemisphere's polar belt for the second time.

Lorentzen et al., 2002 and Baker et al., 2017) and galactic cosmic radiation are also captured (Klecker et al., 1995, Cummings et al., 1993 and Baker et al., 2017).

1.1.3 *South Atlantic Anomaly*

In the inner Van Allen belt of the shifted and tilted dipole nature of the Earth's magnetic field – the magnetic field axis is tilted by about 11 degrees with respect to the Earth's rotational axis, a region with a weak magnetic field is produced (Figure 1.4). It is particularly weakest over Brazil and extends into the South Atlantic region, hence the name South Atlantic Anomaly (Cain, 1967, Baker et al., 2017).

Trapped particles, mainly high-energy protons, approach the Earth's surface up to an altitude of about 200–300 kilometres due to mirroring along the magnetic field

lines. As a consequence, this is the region where spacecraft on LEO encounter the most intense particle flux (Baker et al., 2017).

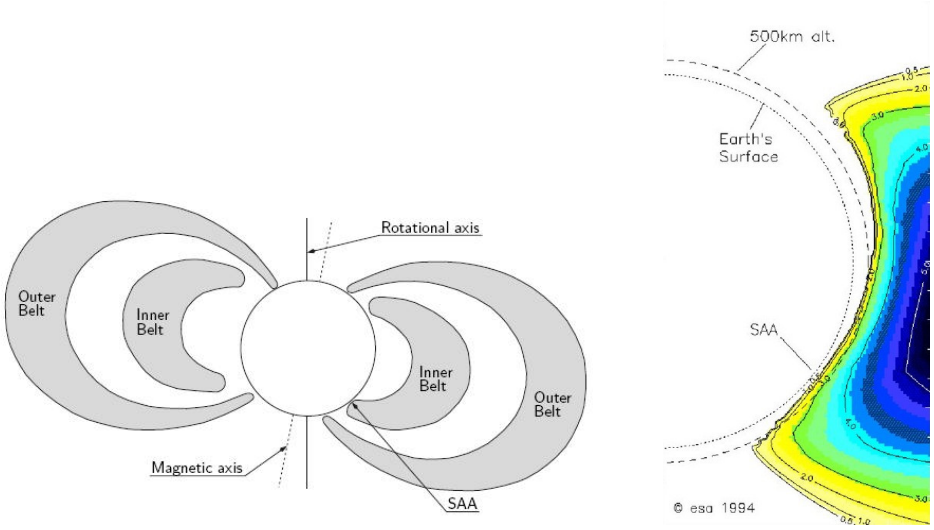

Figure 1.4: South Atlantic Anomaly as a tip of the inner Van Allen Belt. Right Figure from ESA, 2024 and left Figure from Métrailler, 2019.

1.2 TRAPPED PARTICLE BACKGROUND MODELS

Since the discovery of the Van Allen radiation belts, the harmful effect of an intense population of penetrating particles on electronic systems, the structural material of spacecraft, and people in space has been recognized (Allen, 1966, Baker et al., 2017). This motivated the development of radiation belt models, which became an essential part of planning future missions.

1.2.1 *AE8/AP8 Models*

In the 1960s and 1970s NASA developed AE8/AP8 (Vette, 1991, Sawyer and Vette, 1976 and Fung, 1996) models based on data from 24 satellites. These data were collected over two solar cycles, measuring the average electron and proton fluxes for the solar minimum and maximum. The energy range for electrons is 0.04 MeV-7 MeV, and for protons, 0.1 MeV-400 MeV. AE8/AP8 models have been used for decades, but some limitations and inaccuracies are known. For example, they are too simplistic and only provide average values for only two stages of solar activity. Another problem is that it does not provide any statistical methods, such as error bars, to estimate the potential risk (Soria-Santacruz Pich et al., 2017).

1.2.2 *AE9/AP9 Models*

To address these issues with the AE8/AP8 models, The National Reconnaissance Office (NRO) and the Air Force Research Laboratory (AFRL) supported the development of the AP9/AE9 (Ginet et al., 2013) models. These models were based on over 37 data sets from 1976 to 2011 and cover three solar cycles. The advantage of the models is that both ends of the energy ranges have been extended so that the range for electrons is 1 keV-10 MeV, and for protons is 1.15 keV-2 GeV. Another advantage of the model is that it is based on Monte Carlo simulation, which can provide averages and percentiles and quantify the uncertainty due to space weather variability (Soria-Santacruz Pich et al., 2017).

1.2.3 *Comparative Analysis of Trapped Particle Models*

Over the years, several studies have been comparing these models with each other or with other measured data. In this section, we present two of them as examples.

The study Řípa et al., 2020 focused, among other things, on the comparison of the integral fluxes given by the AE9 50% confidence level (CL) and AE8 MAX models of captured electrons, as well as the comparison of the integral fluxes given by the AP9 50% CL / AP8 MIN models of captured protons. MIN and MAX refer to the solar minimum and maximum. The comparison of these models is expressed using the flux ratios. The analysis was performed on twelve different values of the inclination (0°, 5°, 10°, 15°, 20°, 30°, 40°, 50°, 60°, 70°, 80° and 90°) and three different values of altitude (500, 550 and 600 km). As shown in Figure 1.5, the Ax8 models give significantly different values of the fluxes of trapped particles, especially for low inclinations and low energies.

Furthermore, Řípa et al., 2020 also compared AP8 MIN and AP9 Mean models with in-situ measurements from BeppoSAX. This section focused on the SAA region at three altitudes (474, 548, and 597 km), with an inclination below 5° and a protons' energy threshold of 20 MeV. As we can see in Figure 1.6, it turns out that the AP8 model underestimates the actual particle flux while AP9 overestimates it, so the BeppoSAX measurements lie somewhere in between.

As an additional example, the study by Soria-Santacruz Pich et al., 2017 analysed proton data ranging from 27.5 MeV (differential) and >97 MeV (integral) obtained from the Jason-2 satellite and compared them to the AP8 MIN and AP9 MC 5th, 50th, and 95th percentiles, where MC stands for Monte Carlo. Jason-2 carries the ICARE-NG (Influence sur les Components Advancés des Radiations de l'Espace-Next Generation (Maget et al., 2014)) instrument on board, which measures the population of electrons and protons in the energy ranges 1.6—3.6 MeV and 27.5-–290 MeV, respectively. However, their research only analyses proton data obtained from this satellite. Jason-2 orbits

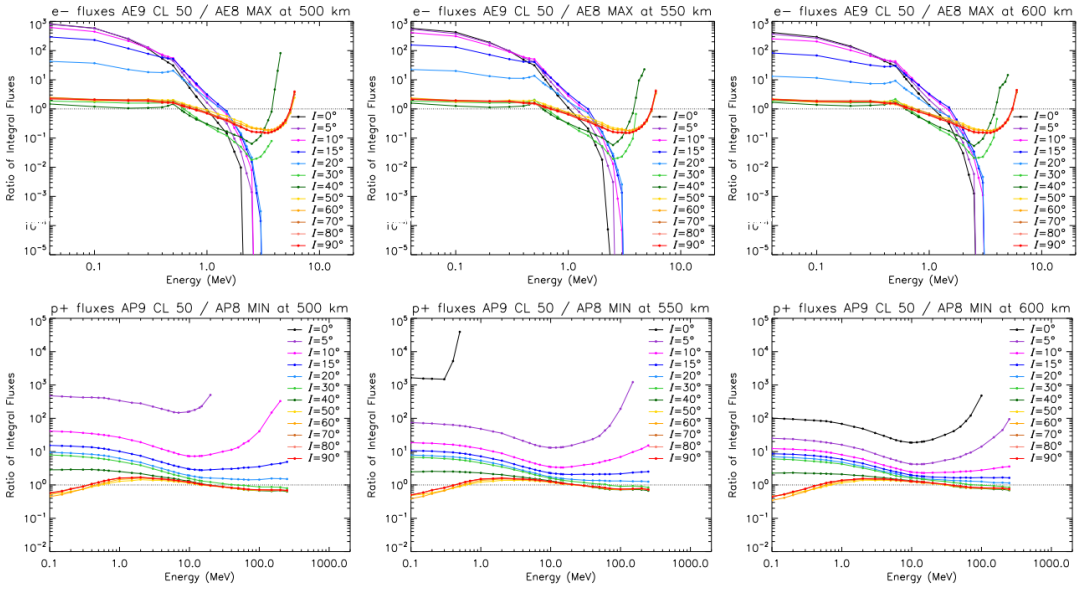

Figure 1.5: *First row*: Ratio of integral fluxes of trapped electrons (AE9 50% CL / AE8MAX). *Second row*: Ratio of integral fluxes of trapped protons (AP9 50% CL / AP8MIN). Columns arranged from left to right represent altitudes 500, 550 and 600 km, respectively. Each image shows the analysis for different inclinations I. Figure from Řípa et al., 2020.

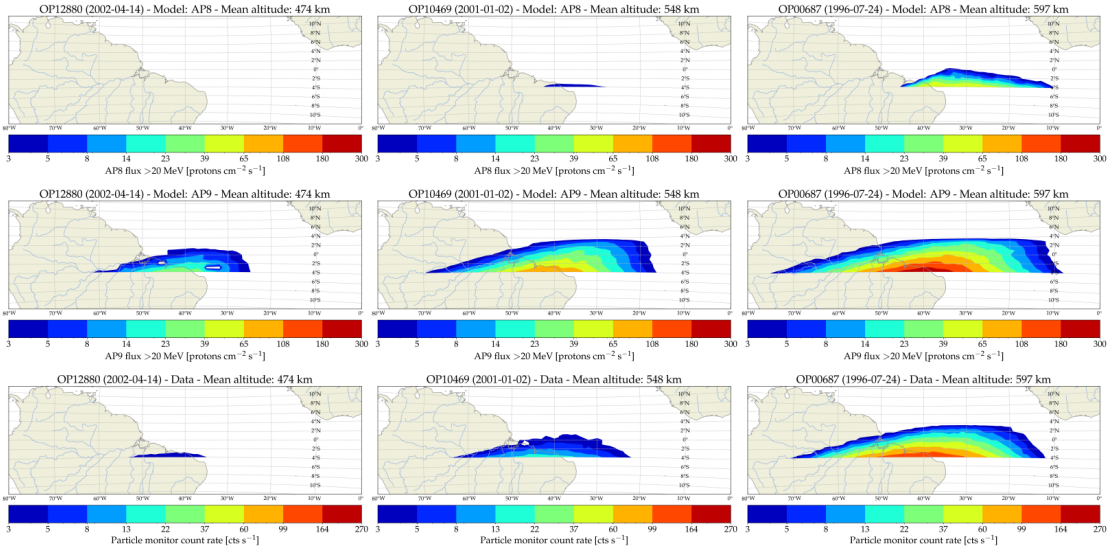

Figure 1.6: Comparison of trapped proton fluxes in the South Atlantic Anomaly by the AP8 MIN (top panels) and AP9 mean (middle panels) models, with the count rate measured by the particle monitor on the BeppoSAX satellite (bottom panels), with an energy threshold of 20 MeV at altitudes of 474 km (left), 548 km (middle), and 597 km (right). Figure from Řípa et al., 2020.

in LEO with an altitude of 1,336 km and an inclination of $\sim 66.0^{\circ}$. Figures 1.7 *(a)* and 1.7 *(b)* show that the AP8 model matches the measured data for both proton channels (27.5 MeV and >97 MeV), but the estimates of all AP9 models are much higher. Additionally, in images 1.7 *(c)* and 1.7 *(d)*, which show the differential and integral fluence spectra, we can see that AP8 MIN almost coincides with the measured data, while all AP9s show much higher values at all energies.

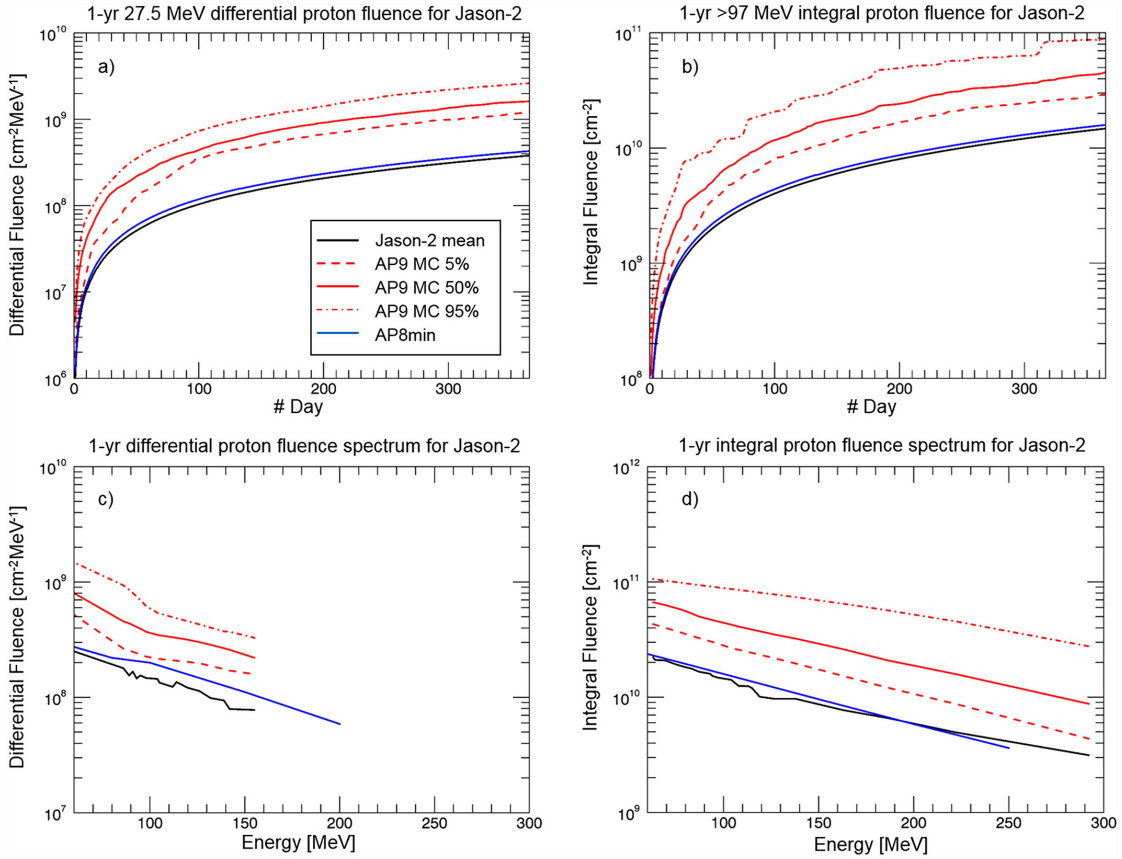

Figure 1.7: The plots show the accumulation of protons as a function of time (i.e., fluence) from Day 1. *(a)* Comparison between Jason-2 proton fluence 27.5 MeV and the models. *(b)* Comparison between Jason-2 proton fluence >97 MeV and the models. *(c)* Jason-2 differential fluence spectrum. *(d)* Jason-2 integral fluence spectrum. Figure from Soria-Santacruz Pich et al., 2017.

Furthermore, Soria-Santacruz Pich et al., 2017 also looked at SAA in relation to the distribution and intensity of protons. They compared the mean of the measured data for the >97 MeV proton channel shown in Figure 1.8 *(a)* by making the ratio of the mean throws from the models to the measured data. Figure 1.8 *(b)* shows the ratio of the AP9 model mean to measured data, and Figure 1.8 *(c)* shows the ratio of the AP8 model mean to measured data. Figures 1.8 *(b)* and 1.8 *(c)* show that the AP9 model

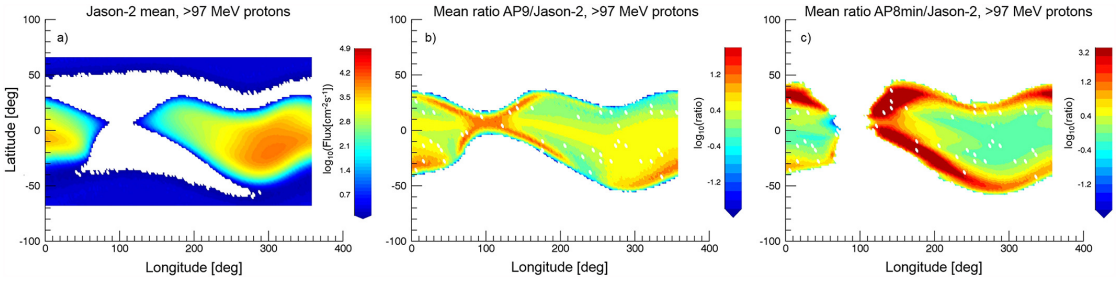

Figure 1.8: *(a)* Jason-2 time-averaged measurements of the SAA (>97 MeV proton data). *(b)* Ratio of AP9 MC mean to Jason-2. *(c)* Ratio of >100 MeV protons from AP8min to Jason-2. Figure from Soria-Santacruz Pich et al., 2017.

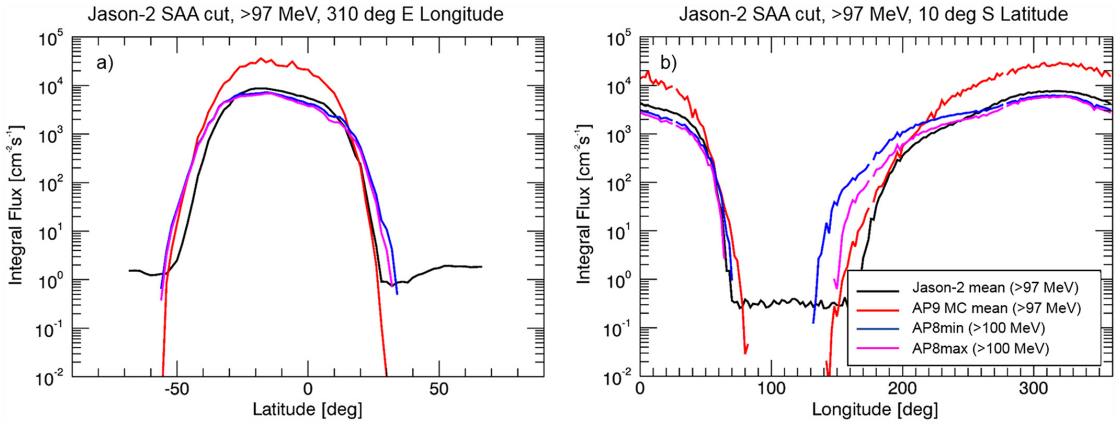

Figure 1.9: Jason-2 time-averaged measurements of SAA compared to model outputs for >97 MeV protons (and for >100 MeV protons in the case of AP8). *(a)* SAA cut through the 310°E longitude. *(b)* SAA cut through 10°S latitude. Figure from Soria-Santacruz Pich et al., 2017.

better reproduces the overall shape of the SAA because the AP8 model predicts a larger size of the SAA, but the AP8 model better interprets the peak flux.

Next, they looked at the SAA as a function of latitude and longitude, as shown in Figure 1.9. Here, we see that the AP9 model better constrains the latitudinal width of the SAA. However, the AP8 model better constrains its peak proton flux.

Part II

METHODOLOGY

2

DATASETS

2.1 GRBALPHA SATELLITE

GRBAlpha is a 1U CubeSat (Figure 2.2), i.e. a cube with a volume of $10 \times 10 \times 10$ cm^3. A Soyuz-2.1a rocket launched it into a sun-synchronous orbit at 550 kilometres from Baikonur on March 22, 2021. The inclination of the orbit is 97.5 degrees, and one complete orbit around the Earth takes about 95 minutes. With its on-board gamma-ray detector, capable of detecting hard X-ray/gamma transient sources such as gamma-ray bursts (GRBs), it serves as a pathfinder for the future CAMELOT constellation of nanosatellites (Werner et al., 2018). The primary objectives of the GRBAlpha mission are to demonstrate the detector concept in space, to verify the detector's lifespan, and to measure background levels in low-earth orbit, including regions within the outer Van Allen radiation belt and the South Atlantic Anomaly (Řípa et al., 2022).

2.1.1 *Description of detectors*

Electrons in insulators or semiconductors only have three bands of energy available to them: the valence, conduction, and forbidden bands. When energy is absorbed, an electron can jump from the valence to the conduction band. However, the return of an electron to the valence band with the emission of a photon is inefficient in a pure crystal. Furthermore, the resulting photon would have too much energy to fit into the visible spectrum due to the typical widths of the gaps. Inorganic scintillators commonly contain small amounts of impurities called activators to increase the probability of visible photon emission during deexcitation. The result is the formation of energy states within the forbidden gap, which allows the electron to de-excite back into the valence band (Knoll, 2010).

A charged particle passing through the detection medium will form many electron-hole pairs due to electron excitation. The positive hole will quickly ionize the activator. Meanwhile, the electron moves freely through the crystal until it encounters an ionized activator. If the excited configuration with an allowed transition to the ground state occurs, there is a high probability of deexcitation, which can result in the emission of a visible photon (Knoll, 2010).

These optical photons are then detected by silicon photomultipliers (SiPMs), in particular with the Multi-Pixel Photon Counters (MPPCs). When an optical photon collides with a silicon atom, it produces an electron-hole pair. The strong electric field

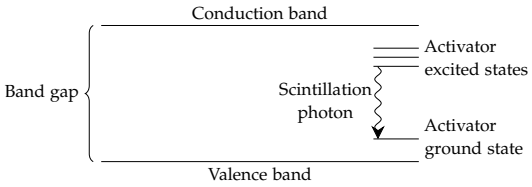

Figure 2.1: Energy band structure of an inorganic crystal with activator. Redrawn from Knoll, 2010.

inside the photodiodes accelerates this pair, generating secondary electron-hole pairs and causing a chain reaction. This chain reaction amplifies the output current. Ideally, each photodiode should collide with a maximum of one photon, and the number of photodiodes contributing to the output signal and amplitude is proportional to the number of scintillation photos. The signal generated in MPPC is converted to a voltage signal and measured by pulse height in the pre-amplifier and shaping amplifier. Finally, the output is converted to digital form using an analogue-to-digital converter (ADC) (Dafčíková, 2022).

The onboard GRBAlpha detector features a $75 \times 75 \times 5$ mm CsI scintillator with Tl activator read out by eight multi-pixel photon counters, divided into two independent readout channels with four MPPCs per channel (Řípa et al., 2022). Pre-launch calibration with different radioactive isotopes provided the conversion between the spectral channel and energy:

$$\mathrm{E} = \mathrm{gainfactor} \cdot \mathrm{ADC\_ch} + \mathrm{offset}, \tag{2.1}$$

where ADC_ch is the ADC channel, and the offset is -154 keV. The initial gain factor was set to 4.08 keV/ch. However, after about two years on orbit, a detector's gain degradation was noticed by measuring the activation lines following GRBAlpha's passage through the SAA. A new gain factor of 4.31 keV/ch was established. Originally, the threshold for the first energy band was set at 30 keV. Due to the gradual degradation of the detector, it was increased to 70 keV. Table 1 shows the approximate energies for the energy bands.

2.2 VZLUSAT-2 SATELLITE

The VZLUSAT-2 CubeSat is 3U in size (Figure 2.2) and was developed by the Czech Aerospace Research Centre as a technology mission. On January 13, 2022, a Falcon 9 rocket launched the satellite from Cape Canaveral to a 550 km altitude and with the same inclination as GRBAlpha. Its primary payload consists of two Earth-observing cameras and two GRB detectors are also among several secondary payloads. Both detectors, along with $75 \times 75 \times 5$ mm CsI(Tl) scintillators, work on the same principle as on GRBAlpha. However, detectors are placed under custom solar panels with a reduced copper layer for better X-ray transparency (Řípa et al., 2022). The gain factor for

	GRBAlpha	VZLUSAT-2
ADC ch.	E [keV]	
0–256	∼ (70–950)	∼ (30–890)
64–256	∼ (115–950)	∼ (110–890)
128–256	∼ (385–950)	∼ (370–890)
192–256	∼ (650–950)	∼ (630–890)

Table 1: The table contains four energy bands defined by ADC channels (ADC values of pulse height) and corresponding energies in keV for GRBAlpha and VZLUSAT-2.

VZLUSAT-2 was chosen the same as on GRBAlpha, based on the preliminary laboratory measurements, at 4.08 keV/ch, and the threshold for the first energy band stayed at 30 keV. Energies for the energy bands are listed in Table 1.

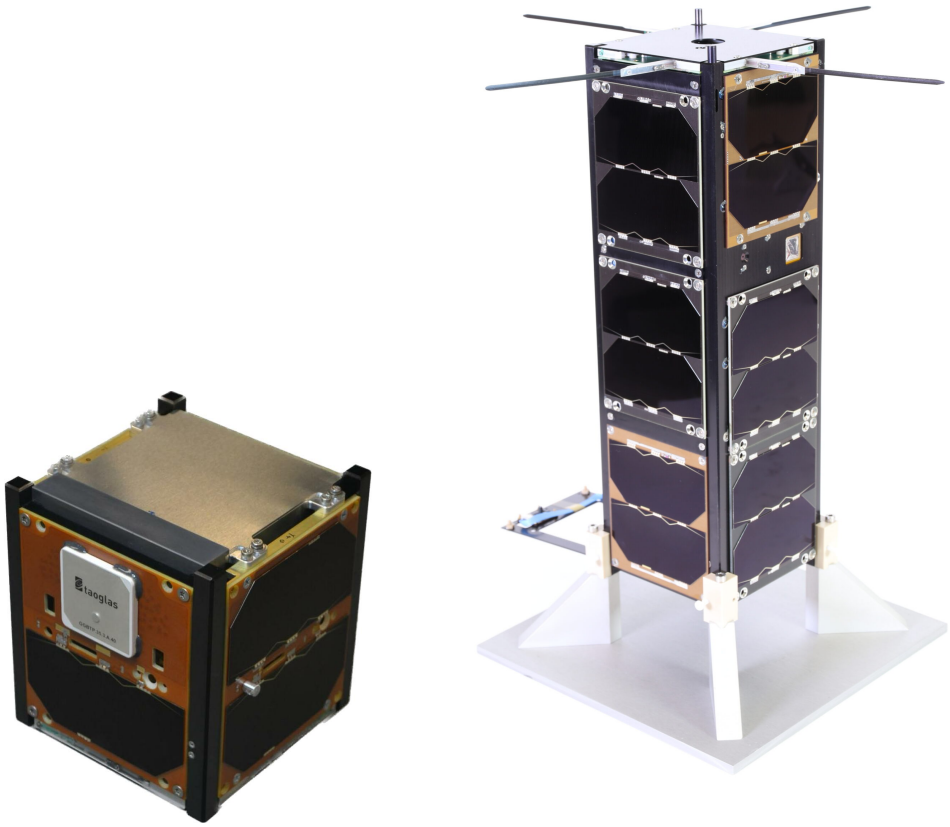

Figure 2.2: Satellites GRBAlpha on the *left* (from web GRBAlpha, 2024) and VZLUSAT-2 on the *right* (from web VZLUSAT-2, 2024).

2.3 DATA SELECTION

Data from satellites GRBAlpha and VZLUSAT-2 are collected with several exposure values, which determine the resolution of the light curves. The most common data have an exposure of 4 or 1 second and were used for our research work. However, data with a 60-second exposure, which are used to characterize the long-term degradation of the detector, are the second most common.

The maps for VZLUSAT-2 were created using data collected from February 2022 to December 2023. The dataset of both detectors consists mainly of files with a 1-second exposure. Only a few files (5 in total) have a 15-second exposure, and two files have a 4-second exposure. The lowest energy band has an instrumental noise peak, so we had to filter out data with a threshold lower than 45 ADC in that band.

The maps for GRBAlpha were created using data collected between April 2021 and November 2023. Data with exposures longer than 4 seconds were filtered out. Most data points in the dataset have an exposure of 1 second. We filtered out data with a threshold lower than 52 ADC in the lowest band.

The data for the trigger algorithm were collected from the GRBAlpha satellite from April 2021 to January 2024, and all data points had a one-second exposure. Again, a threshold of 52 ADC was set in the lowest band.

3

DATASETS AND BACKGROUND MODELS EXAMINATION

When attempting a quantitative analysis of the data from satellites GRBAlpha and VZLUSAT-2, we encounter several problems. The first is that the detector can become saturated when a satellite passes through a high-energy region, making it difficult to determine the actual flux values in these regions. The satellite's uncontrollable rotation is another cause of inaccuracy in determining the actual particle flux. Finally, the lack of information about the response matrix for charged particles also prevents a deeper understanding of how the detector interacts with particles arriving at different energy levels and angles.

However, this study focuses on a visual comparison of the predictive models and data measured by the GRBAlpha and VZLUSAT-2 satellites. Visual comparison can show us many agreements and disagreements between models and measured data. For this purpose, we have found the `HEALPix` (Gorski et al., 2005) software to be the most helpful tool. To achieve this pixelization, we use `healpy`, which is a Python library that wraps around `HEALPix`.

3.1 VISUALISATION USING HEALPIX

`HEALPix` is an acronym for Hierarchical, Equal Area, and isoLatitude Pixelation of a sphere. This tool was developed to have a mathematical structure which supports a suitable discretization of functions on a sphere at sufficiently high resolution and for fast and accurate analysis of huge full-sky data sets (Motalebi, 2020).

It consists of three key parameters:

- **Resolution:**
  According to Gorski et al., 2005, a `HEALPix` map has N_{pix} pixels of the same area Ω_{pix}.

$$N_{\text{pix}} = 12N_{\text{side}}^2 \tag{3.1}$$

$$\Omega_{\text{pix}} = \frac{\pi}{3N_{\text{side}}^2} \tag{3.2}$$

  The base resolution comprises twelve pixels arranged into three rings around the equator and poles. Parameter N_{side} defines the number of divisions along each side of each of the 12 base-resolution pixels, so it defines the needed resolution,

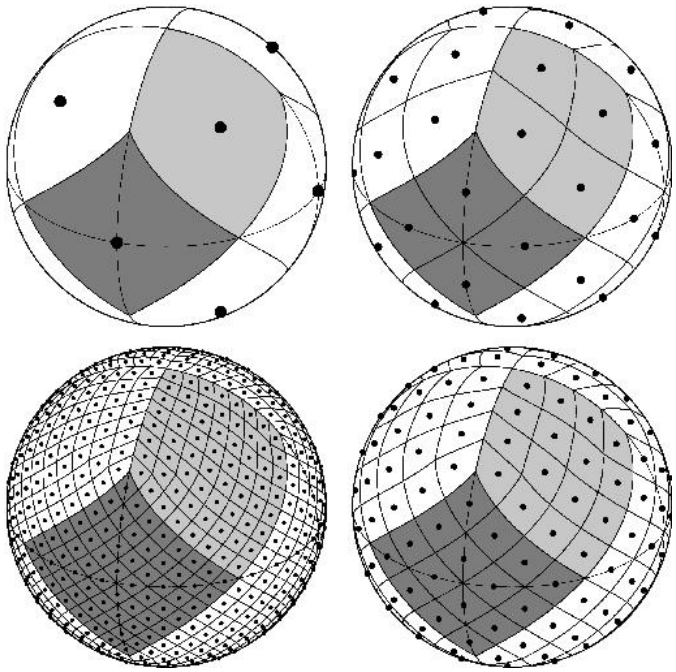

Figure 3.1: Moving clockwise from *top left*: HEALPix pixelation of the sphere for resolutions N_{side} = 1, 2, 4, 8, and total number of pixels N_{pix} are 12, 48, 192 and 768. Figure from Gorski et al., 2005.

as shown in Figure 3.1. All pixels have the same surface area, so the angular resolution is defined as:

$$\theta_{pix} \equiv \sqrt{\Omega_{pix}} \tag{3.3}$$

$$= \sqrt{\frac{1}{3\pi}} \cdot \frac{180}{N_{side}} \tag{3.4}$$

- **Pixel index:**
  Gorski et al., 2005 further explains the methodology of the pixelation. All pixel centres are placed on rings of constant latitude and are equidistant in azimuth. Their positions are defined by $(z \equiv \cos\theta, \phi)$ where $\phi \in [0, \pi]$ is the colatitude in radians measured from the North Pole and $\theta \in [0, 2\pi]$ is the longitude in radians measured eastward. The pixel index $p \in [0, N_{pix}]$ run around those rings can be used for ordering.
- **Ordering scheme:**
  In addition, Gorski et al., 2005 shows that HEALPix supports two different numbering schemes for the pixels, as illustrated in Figure 3.2.

In our case, we have selected these parameters as RING ordering and N_{side}=32.

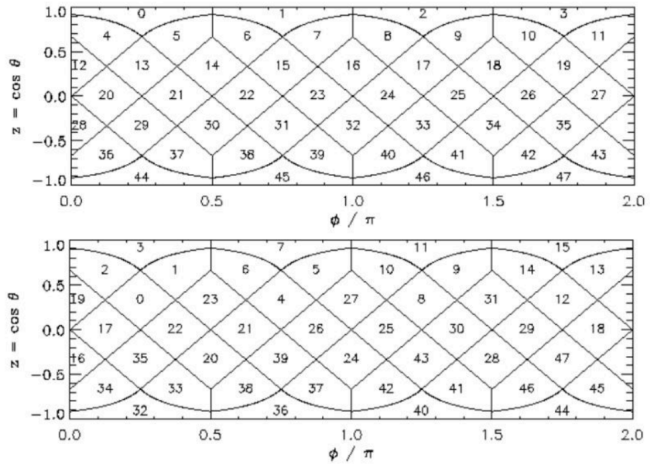

Figure 3.2: RING (*top*) and NESTED (*bottom*) pixel ordering schemes from `HEALPix`. Figure from Gorski et al., 2005.

3.2 TRAPPED PARTICLE BACKGROUND MODELLING FOR SATELLITES

The background radiation environment for satellites GRBAlpha and VZLUSAT-2 was modelled using Irene software (Johnston et al., 2014) version 1.57.004. Firstly, we describe the parameters standard for both satellites and models, AP8/AE8 and AP9/AE9. We have set the inclination to 89 degrees to get the broadest range of latitudes for maximum coverage. We have chosen a Keplerian orbit with the J2 effect to consider Earth's oblateness (Řípa et al., 2020). The J2 effect is the perturbative acceleration caused by the Earth's oblateness, and it is the primary perturbative acceleration for LEO orbits (Wright, 2008). Furthermore, we calculated the mean integral flux assumed to be omnidirectional with the time sampling every 10 seconds. Sampling at 10-second intervals was dictated by the resolution of our maps and the angular velocity of GRBAlpha. With a resolution of 1.83 degrees per pixel, and given that GRBAlpha traverses an angular distance of 0.66 degrees in 10 seconds, we chose this sampling to capture enough data points. MAX condition corresponding to the maximum of the solar cycle was selected for the models. The different parameters used for the GRBAlpha and VZLUSAT-2 satellites were altitude and four different energy levels for protons and electrons. As shown in Figure 3.3, the altitude of GRBAlpha dropped by 43 km between July 2021 and January 2024. Therefore, we selected the middle value from this interval and subsequently divided the compared data into two periods: before and after GRBAlpha dropped to this altitude. GRBAlpha radiation background modelling altitude was 525 kilometres, whereas VZLUSAT-2 was 517 kilometres. Based on Table 1 in Chapter 2, the electron and proton levels in the background modelling of the two satellites differ due to energy band ranges. For GRBAlpha, these are 0.07, 0.115, 0.384, and 0.652 MeV for electrons and 0.1, 0.115, 0.384, and 0.652 MeV for protons. VZLUSAT-2's energies

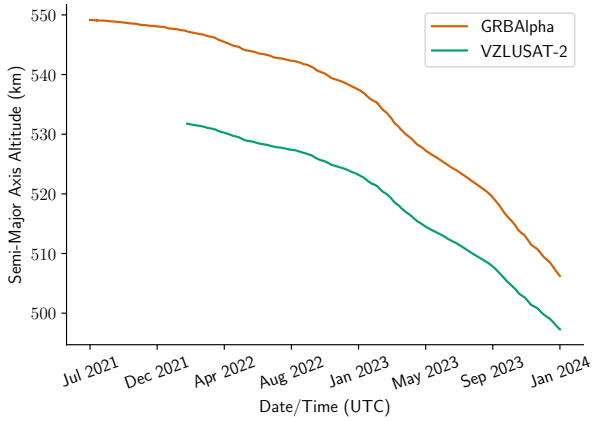

Figure 3.3: The graph represents an altitude decay of GRBAlpha and VZLUSAT-2 satellites from their initial positions to the end of January 2024. Altitude data sourced from Celestrak's (Kelso, 2024) satellite catalogue .

are 0.04, 0.107, 0.368, and 0.629 MeV for electrons and 0.1, 0.107, 0.368, and 0.629 MeV for protons. The background modelling spanned from April 17, 2021, to November 22, 2023, for GRBAlpha and from February 5, 2022, to December 21, 2023, for VZLUSAT-2.

3.2.1 *Trapped Particle Radiation Models of GRBAlpha Orbit*

Models for four energy levels of the GRBAlpha satellite at an altitude of 525 kilometres, with particle flux levels of 10^2, 10^3, and 10^5 (particles per square centimetre per second), are shown in Figures 3.4, 3.5, 3.6, and 3.7. The models corresponding to trapped electrons are represented by Figure 3.4 for model AE8 and Figure 3.5 for the AE9 model. A comparison of these figures shows differences in the predicted radiation environment at this altitude. The AE9 model predicts wider regions with higher electron fluxes in the South Atlantic Anomaly (SAA) than the AE8 model. Conversely, for the outer Van Allen belts, the AE9 model predicts this region to be slightly narrower than the AE8 model. The models corresponding to trapped protons are shown in Figure 3.6 for AP8 and Figure 3.7 for model AP9. Focusing on the SAA, we see the same trend in the predictions as for the electron fluxes.

3.2.2 *Trapped Particle Radiation Models of VZLUSAT-2 Orbit*

We performed a similar analysis for the VZLUSAT-2, which has an altitude of 517 kilometres. Models for electron fluxes are shown in Figure 3.8 for AE8 and Figure

3.9 for AE9, while models for proton fluxes are illustrated in Figure 3.10 for AP8 and Figure 3.11 for AP9. Despite the slight shift in altitude, the predicted radiation environments show analogous patterns as for GRBAlpha.

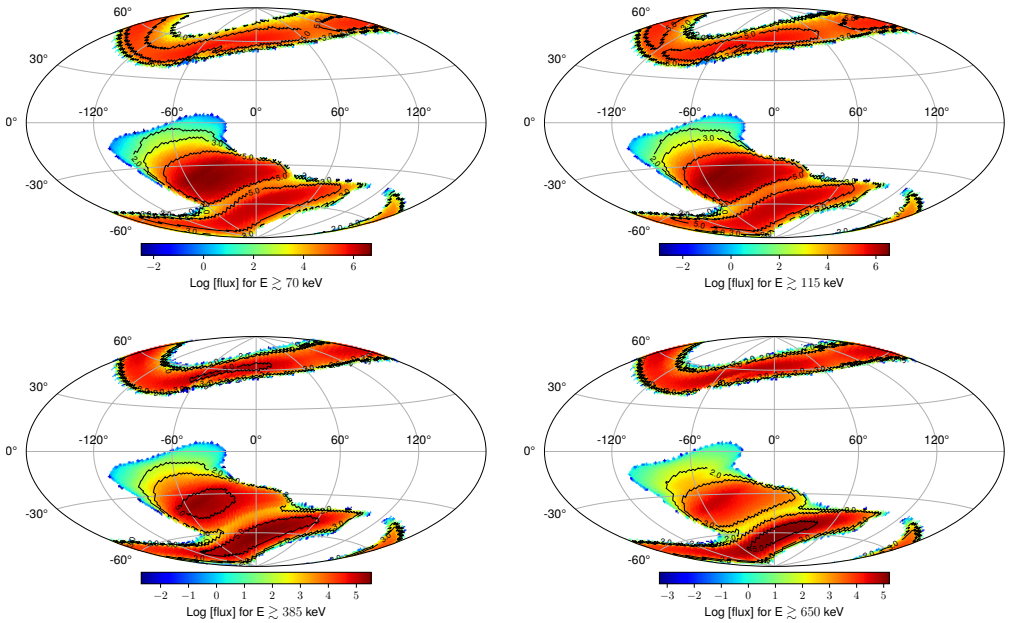

Figure 3.4: AE8 model of particle flux($e^{-}cm^{-2}s^{-1}$) for GRBAlpha's altitude (525 km) at solar maximum across four energy bands. Contours mark the particle flux of levels of $10^2, 10^3$, and 10^5 ($e^{-}cm^{-2}s^{-1}$).

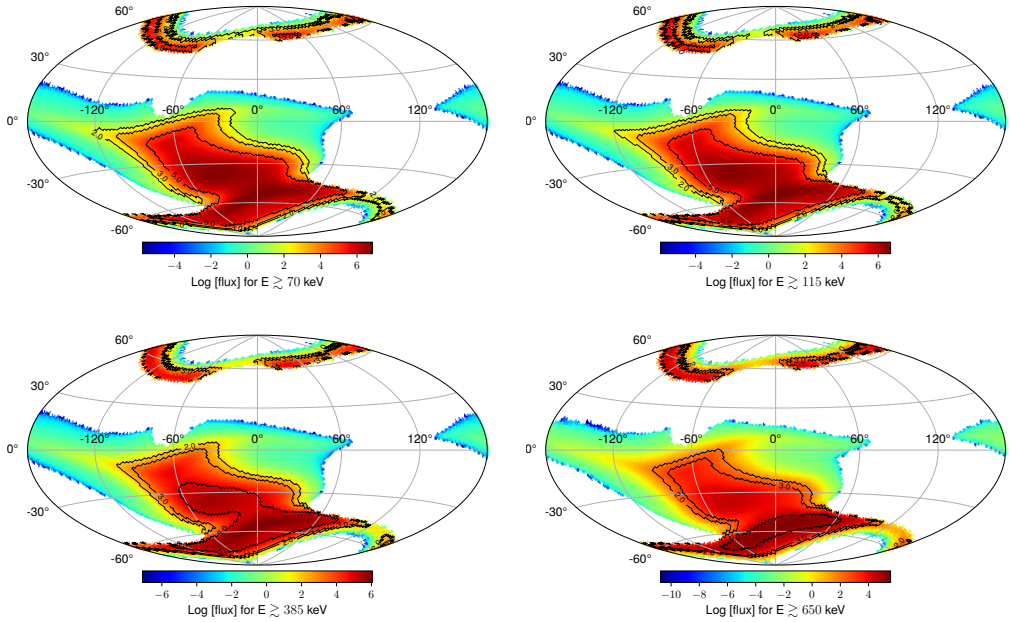

Figure 3.5: AE9 model of particle flux($e^{-}cm^{-2}s^{-1}$) for GRBAlpha's altitude (525 km) at solar maximum across four energy bands. Contours mark the particle flux of levels of $10^2, 10^3$, and 10^5 ($e^{-}cm^{-2}s^{-1}$).

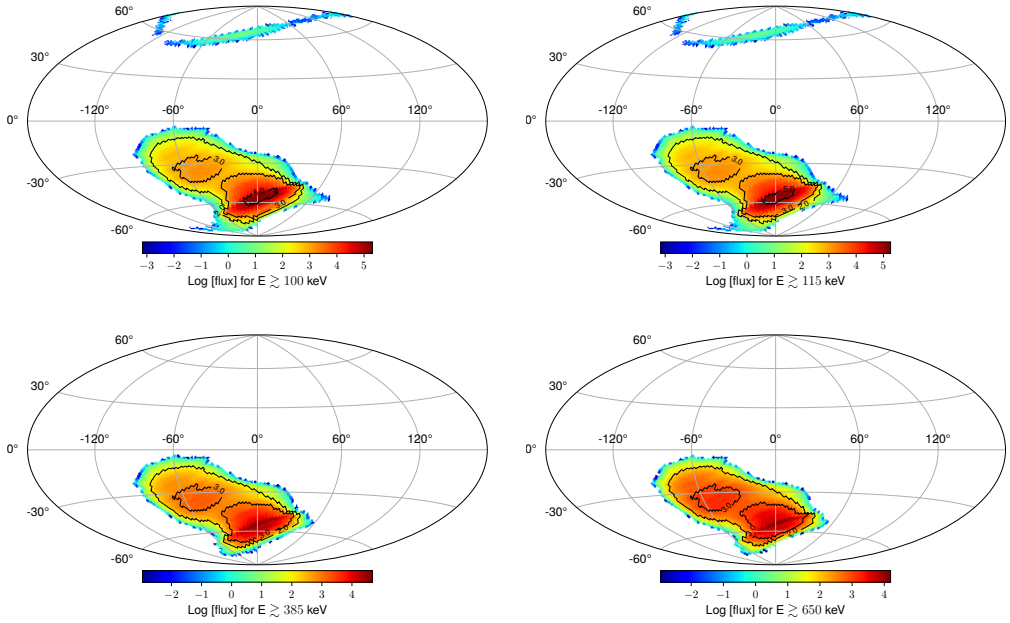

Figure 3.6: AP8 model of particle flux($p^{+}cm^{-2}s^{-1}$) for GRBAlpha's altitude (525 km) at solar maximum across four energy bands. Contours mark the particle flux of levels of $10^2, 10^3$, and 10^5 ($p^{+}cm^{-2}s^{-1}$).

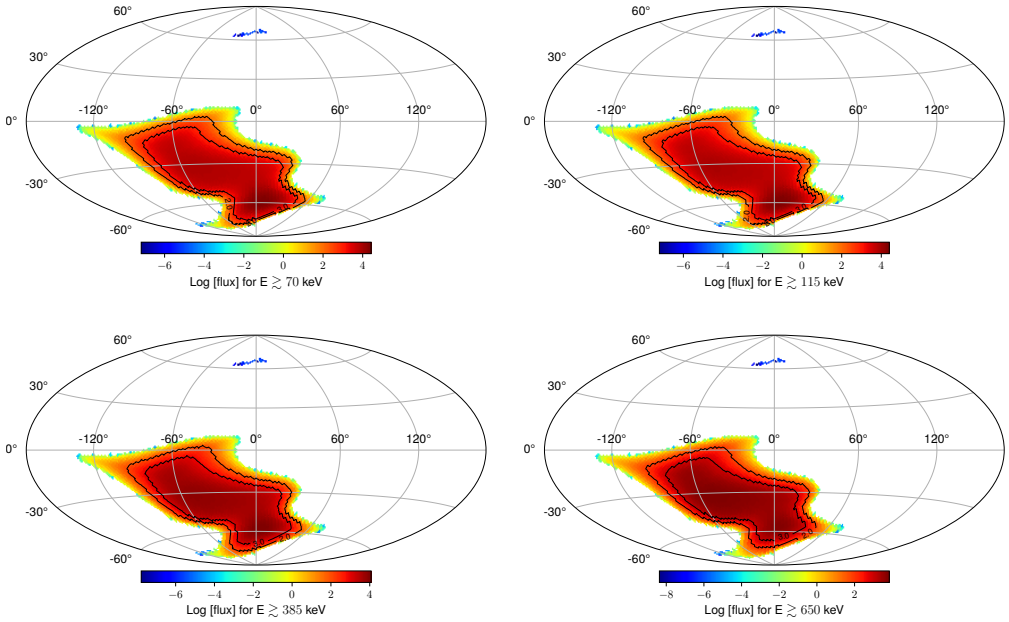

Figure 3.7: AP9 model of particle flux($p^+cm^{-2}s^{-1}$) for GRBAlpha's altitude (525 km) at solar maximum across four energy bands. Contours mark the particle flux of levels of $10^2, 10^3$, and 10^5 ($p^+cm^{-2}s^{-1}$).

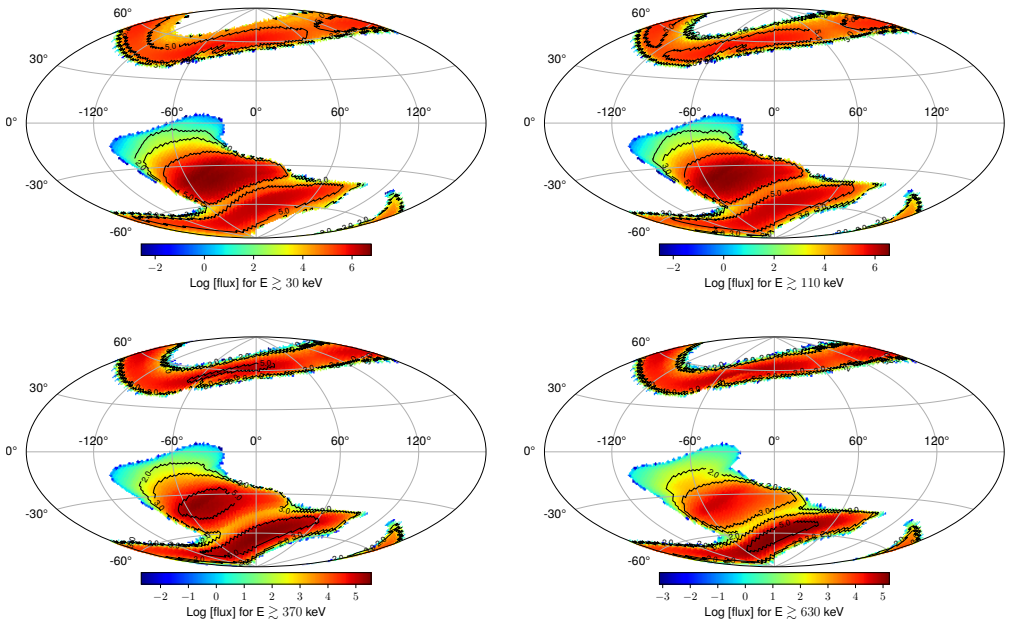

Figure 3.8: AE8 model of particle flux($e^-cm^{-2}s^{-1}$) for an altitude of VZLUSAT-2 (517 km) at solar maximum across four energy bands. Contours mark the particle flux of levels of $10^2, 10^3$, and 10^5 ($e^-cm^{-2}s^{-1}$).

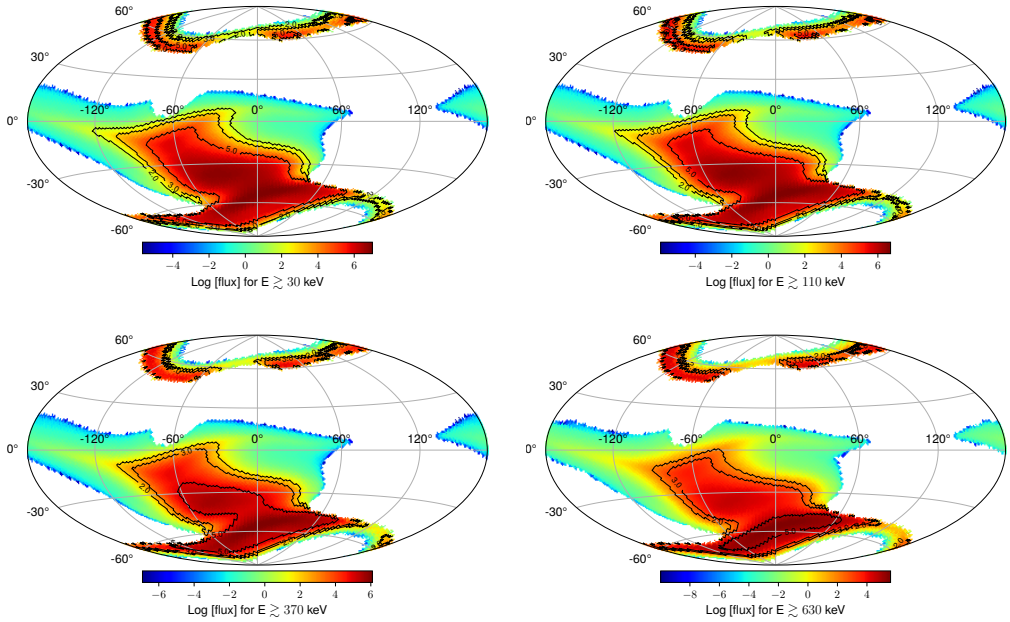

Figure 3.9: AE9 model of particle flux($e^{-}cm^{-2}s^{-1}$) for an altitude of VZLUSAT-2 (517 km) at solar maximum across four energy bands. Contours mark the particle flux of levels of $10^2, 10^3$, and 10^5 ($e^{-}cm^{-2}s^{-1}$).

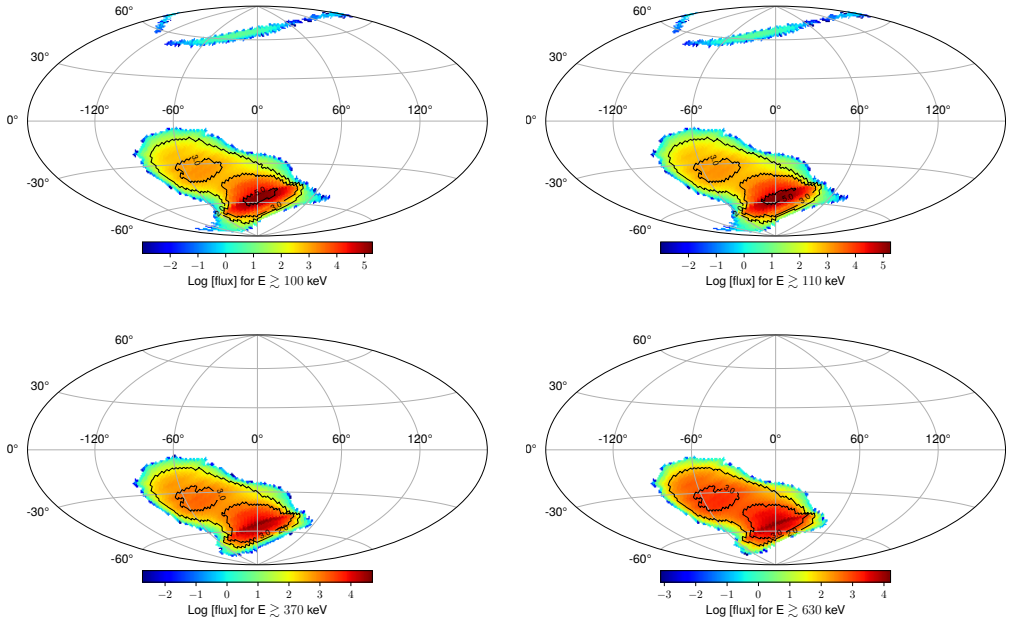

Figure 3.10: AP8 model of particle flux($p^{+}cm^{-2}s^{-1}$) for an altitude of VZLUSAT-2 (517 km) at solar maximum across four energy bands. Contours mark the particle flux of levels of $10^2, 10^3$, and 10^5 ($p^{+}cm^{-2}s^{-1}$).

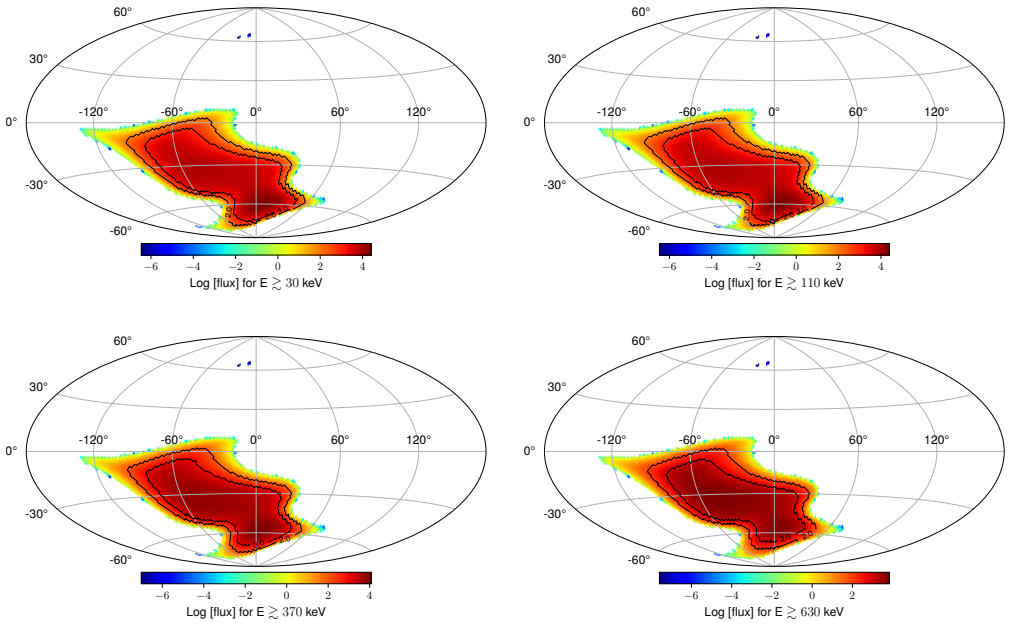

Figure 3.11: AP9 model of particle flux($p^+cm^{-2}s^{-1}$) for an altitude of VZLUSAT-2 (517 km) at solar maximum across four energy bands. Contours mark the particle flux of levels of $10^2, 10^3$, and 10^5 ($p^+cm^{-2}s^{-1}$).

4

TRIGGER ALGORITHM

Studying GRBs from the onset of the prompt gamma emission to the latest possible moment is needed for its deeper understanding. However, continuous light curve saving is impossible because of the instrument's memory constraints. This limitation can be overcome by implementing a triggering algorithm. It determines the essential light curve data to be saved and transmitted for analysis by continuously monitoring the detected count rate and determining the onset of the GRB. The other advantage is that it can quickly notify other satellites and ground-based observatories of the GRB detection.

In this section, we present an overview of a suggested trigger algorithm that can be employed in future CubeSat missions. This trigger algorithm is based on the algorithm developed for the Lomonosov/UFFO-Pathfinder mission (Na et al., 2012 and Jeong et al., 2018). We also specify some of its key parameters based on measured data obtained by GRBAlpha. Furthermore, to avoid numerous false triggers, we used a trigger algorithm to determine regions with rapid background variation corresponding to high background regions, namely polar regions (outer Van Allen Belt) and SAA (tip of the inner Van Allen Belt).

4.1 ALGORITHM OVERVIEW

The trigger mechanism consistently monitors a sudden and significant rise in the count rate. It is quantified by a level of the deviation of the detected signal from the expected background assuming that the detected counts follow the Poisson distribution. Figure 4.2 shows the trigger algorithm block diagram. The algorithm filters detected photons to ensure that only counts within a given energy range are counted through the integration time. As this period ends, counts are transferred to a stack, which is shifted incrementally. The stack is composed of c_1 to c_{n+N} elements. First, n elements ($c_1 - c_n$) are used to calculate the signal S, and next, N elements ($c_{n+1} - c_{n+N}$) for background B. Accumulators S and B sum corresponding elements. However, due to the different numbers of their elements n and N, the obtained value of B is scaled $B=B_o/(N/n)$. For the algorithm to trigger, three conditions must be satisfied. The initial condition is that the stack is filled, indicating that only relevant information about S and B is obtained. The primary condition for S and B is the comparison:

$$(S - B)^2 > kB, \tag{4.1}$$

Trigger windows	W_1	W_2	W_3	W_4
Number of n elements	1	4	16	32
Number of N elements	32	32	32	64
N/n	32	8	2	2

Table 2: Tested trigger time windows with each of the stack elements having a duration of 1s. This is applied to specific energy ranges.

where k is a threshold value that defines the measurement's sensitivity. This equation is then in more detail described by an example in Figure 4.1. The threshold value k is related to standard deviation $\sigma = \sqrt{k}$ because the background has a Poisson distribution. The final condition is that S > B, which ensures that we search for an increase in the signal, not a decrease.

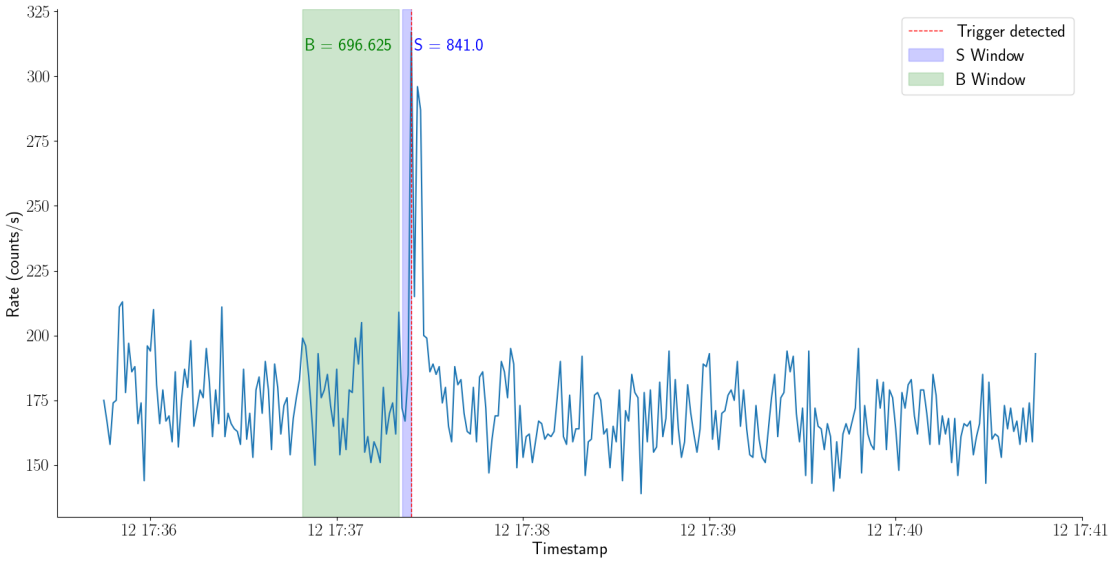

Figure 4.1: The figure shows the light curve of one gamma-ray burst detected by the GRBAlpha satellite (GRB 240112C). The red vertical dashed line indicates the moment of detection for window (4, 32) and k = 20.25. The blue area shows the region from which the signal S is computed; for this particular window, it is four seconds (n = 4). The green area highlights the region from which B_0 is computed and then normalized by $B=B_0/(N/n)$ since the B window has an 8-times longer window (N=32) than the S window. As we can see, B for this case was equal to B = 696.625 and S = 841.0. This gives us a value of $(S-B)^2 = 20844.14$, which is higher than $k \cdot B = 14106.66$, so the triggering condition in the equation 4.1 is satisfied.

The triggering algorithm consists of several sets of energy ranges with pairs of signal and background windows, shown in Table 2, which run in parallel to achieve the detection of a large variety of GRBs.

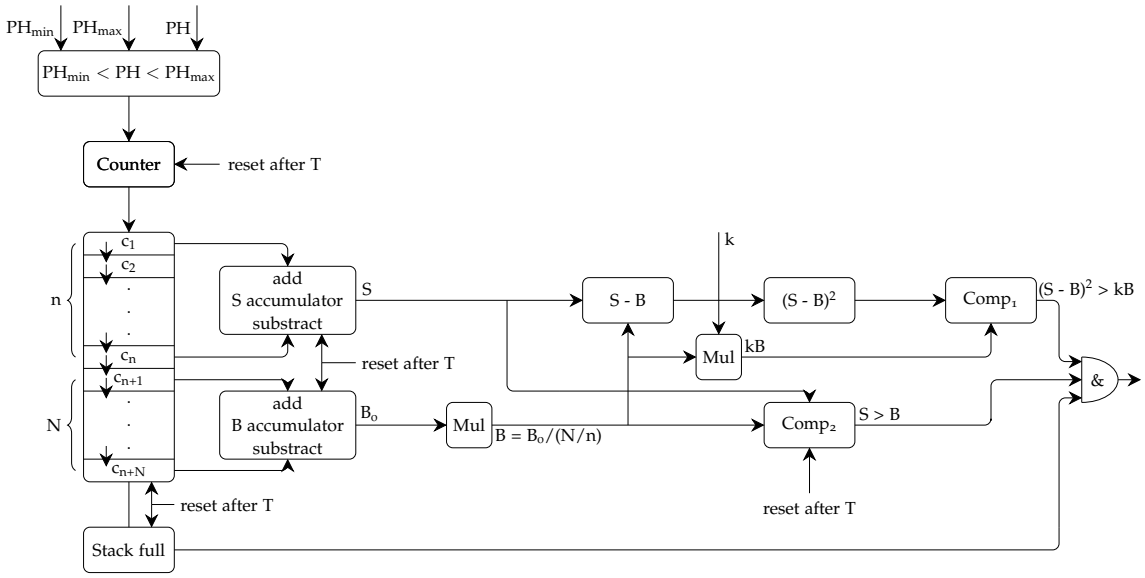

Figure 4.2: Schematic block diagram of the triggering algorithm. Redrawn from Jeong et al., 2018.

5

DATA ANALYSIS AND CLUSTERING

5.1 STATISTICAL ANALYSIS

We used several statistical methods during the creation of the maps, which we describe in this section.

- Mean (μ):

$$\mu = \frac{1}{n}\left(\sum_{i=1}^{n} x_i\right) \tag{5.1}$$

  Since the modelled data has no significant outliers in individual pixels, the mean value accurately describes them. Therefore, we used it to generate the maps of the modelled background.

- Median:

  On the other hand, we had to employ a median to avoid the influence of extreme values in some pixels when plotting the measured data. These extreme values might be the result of undetected solar flares.

  If a dataset has an odd number of values, the median is the middle value of sorted values. If the number of values in the dataset is even, the median is an average of two middle values of sorted values.

- Standard deviation (σ):

  The standard deviation measures the dispersion of the count rates and is defined as:

$$\sigma = \sqrt{\frac{1}{N}\sum_{i=1}^{N}(x_i - \mu)^2} \tag{5.2}$$

- Coefficient of variation (CV):

$$\mathrm{CV} = \frac{\sigma}{\mu} \tag{5.3}$$

  The coefficient of variation is defined as the ratio of the standard deviation to the mean; thus, it provides a normalized measure of dispersion. We used it to determine the variability in individual pixels.

These statistical methods were used as follows:

```
npix = hp.nside2npix(nside)
healpix_values = [[] for _ in range(npix)]

for i in range(len(lonAll)):
    lon = lonAll2[i]
    lat = latAll[i]
    count_rate = rateAll[i]

    pixel_idx = hp.ang2pix(nside, np.radians(90 - lat), np.radians(lon))
    healpix_values[pixel_idx].append(count_rate)

healpix_mean = np.array([np.mean(values) if values else 0 for values in
    healpix_values])
healpix_median = np.array([np.median(values) if values else 0 for values in
    healpix_values])
healpix_std = np.array([np.std(values) if values else 0 for values in
    healpix_values])
healpix_cv = healpix_std/healpix_mean
```

We transformed the longitude and latitude of each observation into corresponding `HEALPix` indices using the function `hp.ang2pix`. For each pixel, we collected all counts that fell within that particular pixel. Then, the list of counts for each pixel is stored in the *healpix_values* array. Only then can the mean, median, standard deviation and coefficient of variation of each pixel count be calculated. We computed them only for pixels with at least one count.

5.2 CLUSTERING WITH HDBSCAN

In the trigger algorithm, we took advantage of the fact that the high-threshold trigger algorithm triggers mainly in areas with high background, and thus the low background has a low detection density. This allows us to use the `HDBSCAN` clustering algorithm to distinguish between low and high background regions.

Hierarchical Density-Based Spatial Clustering of Applications with Noise – `HDBSCAN` (McInnes et al., 2017) is a clustering algorithm that analyses the density of data points. One of the advantages of `HDBSCAN` is that it can effectively extract clusters from non-uniformly dense datasets with noise. The algorithm also requires tuning only of a few parameters and uses its clustering stability index as a reference for the final clustering result (Cui et al., 2021).

To estimate the density of points, `HDBSCAN` uses the parameter *min_samples*. If, for example, the minimum sample size is set to 7, the algorithm calculates the furthest distance a point must travel to reach its closest seven points, known as the core distance

(Figure 5.1). For further analysis, HDBSCAN estimates density by taking the inverse of this core distance. Figure 5.1 shows the relationship between core distance and density – smaller core distances indicate denser regions, while larger ones indicate sparser regions (Thien, 2021).

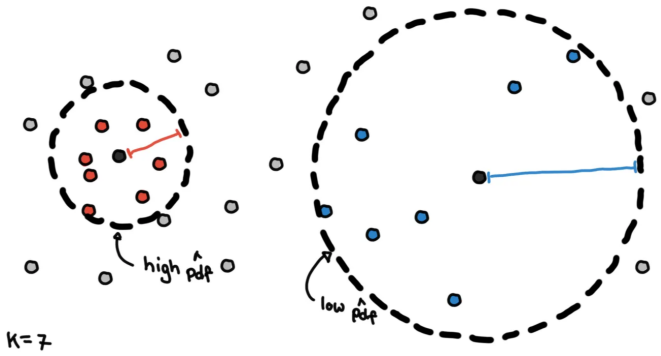

Figure 5.1: Illustration of core distance and density based on parameter *min_samples*. Figure from Berba, 2021.

After finding the core distances of all points, HDBSCAN computes the so-called mutual reachability distance (MRD) between each pair of points using:

$$d_{\text{mreach}-k}(a,b) = \max\left\{\text{core}_k(a), \text{core}_k(b), d(a,b)\right\}, \tag{5.4}$$

where $\text{core}_k(a)$ and $\text{core}_k(b)$ are the core distances of the k *min_samples* of point a and point b, and $d(a,b)$ is the Euclidean distance between point a and point b (Cui et al., 2021).

It then constructs a minimum spanning tree for the dataset using the MRD. The result is a tree that connects all the data points so that the total sum of the mutual reachability distance is as small as possible, as shown in Figure 5.2 (ii).

When the minimum spanning tree is created, HDBSCAN then creates cluster hierarchies. The tree edges are sorted by distance and then connected to clusters by connecting the shortest MRD, as shown in Figure 5.2 (iii). However, this hierarchy may contain a lot of noisy points, so HDBSCAN uses a process called condense down to filter out this noise. In this process, we define the second of the two HDBSCAN's parameters, *min_cluster_size*, which specifies the minimum number of points a cluster must have. The algorithm checks each point where a new cluster is created to ensure it has at least the same number of points as the *min_cluster_size* parameter. If it does, it is considered a valid cluster; otherwise, the data is considered noise. The result is a condensed tree structure, as shown in Figure 5.2 (iv). In visualization, the new measure, lambda, is inversely proportional to distance: $\lambda = \frac{1}{\text{distance}}$.

Finally, HDBSCAN applies the cluster stability index S to determine the final clustering results. The algorithm uses the value of λ to measure the stability of clusters as follows.

For each cluster, it defines a value of λ_{birth}, which is the value of λ when the cluster separates and becomes a cluster itself. It also defines λ_{death} as the value of λ when a cluster splits into smaller clusters if this happens. Next, for each point in each cluster, it defines λ_p value, which is the value at which the point leaves the cluster because each point eventually drops out of the cluster at some point between λ_{birth} and λ_{death} or leaves the cluster when the cluster splits into two smaller ones. The stability of the cluster is further computed:

$$S = \Sigma_{p \in \text{cluster}}(\lambda_p - \lambda_{\text{birth}}) \tag{5.5}$$

The algorithm then 'looks' at Figure 5.2 (iv) starting from the bottom and compares the stability of the clusters. If the sum of the stability of the child clusters is greater than the sum of the parent cluster, the child cluster is selected as the cluster. Conversely, if the cluster stability is greater than the sum of the child clusters, this cluster is selected as the actual cluster. The algorithm continues in this way until it reaches the root node (Leland McInnes, 2016). The selected clusters in the toy model can be seen in Figure 5.2 (v).

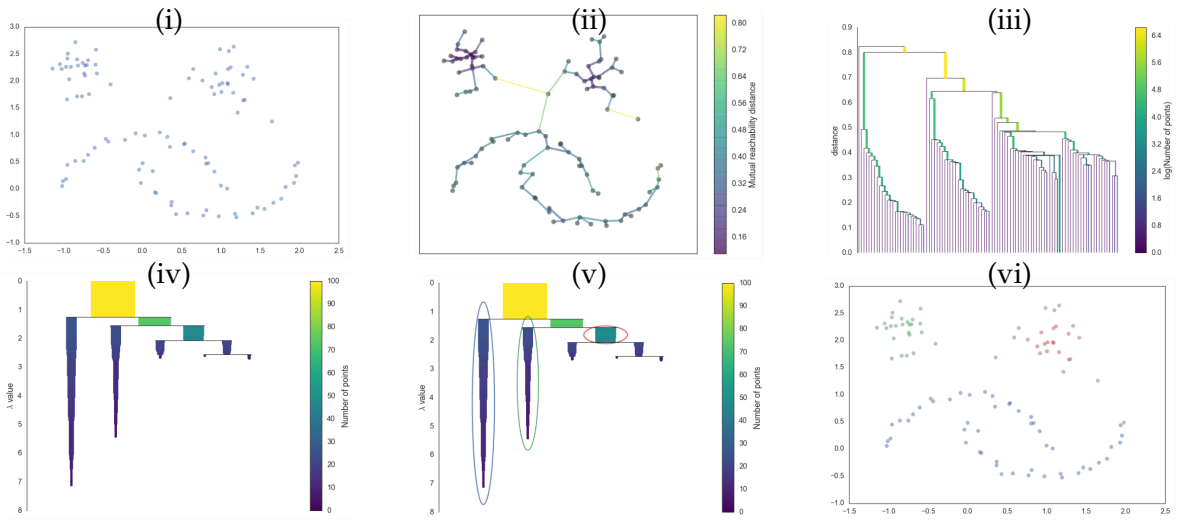

Figure 5.2: The principle of the HDBSCAN algorithm. (i) Visualization of the original data used as an example. (ii) The minimum spanning tree based on mutual reachability distances. (iii) The cluster hierarchy. (iv) Condensed tree structure. (v) Selection of clusters based on stability index S. (vi) Visualization of final determination of clusters. Images are collected from (Leland McInnes, 2016).

Part III

RESULTS & DISCUSSION

6

RESULTS & DISCUSION

6.1 COMPARATIVE ANALYSIS BETWEEN DATA AND MODELS

In this section, we compare the model's particles' flux spatial distribution with the spatial distribution of measured data by two detectors of the satellite VZLUSAT-2 and by the satellite GRBAlpha for two levels of altitude, each for four different energy bands. Comparing the energy bands, we observe that the particle flux across the map decreases as the energy increases. From the overall observation, we found that models cannot perfectly overlap with measured data. The detailed structures inside the Van Allen belts and SAA deviate from the models. However, the AE8 and AP8 models provide valid information about these regions' overall shape and spatial distribution in the two lower energy bands. On the other hand, for the remaining two energy bands in the higher energies, models AE9 and AP9 yield a better description of the overall shape of these regions. An analysis of the data for GRBAlpha at both its initial and lowered altitudes, along with that measured by VZLUSAT-2 for both detectors, led us to similar conclusions.

To be able to do a quantitative analysis, which means a direct comparison of the particle flux values, we propose using the GEANT4 (Geometry and tracking 4) (Agostinelli et al., 2003) simulation tool in the future. By simulating particle transitions through the material of our satellite, we can obtain important information about the actual particle flux and thus compare models and data at this level.

6.1.1 *Comparison with GRBAlpha measurements*

We start by comparing modelled and measured data at GRBAlpha's initial altitude for the first two lowest energy bands, as we can see in Figure 6.1. Looking first at the measured electron flux in the Van Allan Belt in the Northern Hemisphere, we see that its shape closely matches AE8. However, the modelled islands of this belt's most significant electron fluxes differ. Moving to the Van Allen Belt in the Southern Hemisphere, we see that the AE8 model defines the overall shape of the electron flux region less accurately as it predicts a smaller region than measured, although the regions predicted by the model lie within the measured regions. The last region of interest is the South Atlantic Anomaly region. The AE8 model predicts its shape very accurately. The AP8 also captured the overall shape of the proton flux region in the SAA well. However, a

more detailed comparison of the islands with the most significant proton flux within SAA again shows inaccuracies.

The AE9 model provides a less accurate description of Van Allen Belts than the AE8 model on these lower energy bands. It predicts much smaller regions, and the regions it predicts only overlap with the areas of maximum fluxes of measured data but not their total width. Conversely, regarding SAA, both AE9 and AP9 models predict a larger region of higher fluxes. However, the shape of the area of predicted maximum flux nicely overlaps with the total measured SAA region.

Next, we move on to Figure 6.2, which shows the remaining two energy bands with higher energies. Here, the measured data are almost identical to the contours of the AE9 and AP9 models. In contrast, the AE8 and AP8 models predict smaller regions of higher fluxes with maxima that do not align with the actual data.

As can be seen in Figures 6.3 and 6.4, the measured data from the GRBAlpha satellite for lowered altitude appear to be analogous to initial altitude data. Hence, the comparative analysis is identical.

6.1.2 *Comparison with VZLUSAT-2 measurements*

Although comparing models with the VZLUSAT-2 data from both detectors is more challenging due to the limited measured data compared to GRBAlpha, we can still observe that the data sets are almost identical. Therefore, our comparison with the models leads us to the same conclusions, as illustrated in Figures 6.5 and 6.6 for no.0 detector, and in Figures 6.7 and 6.8 for no.1 detector.

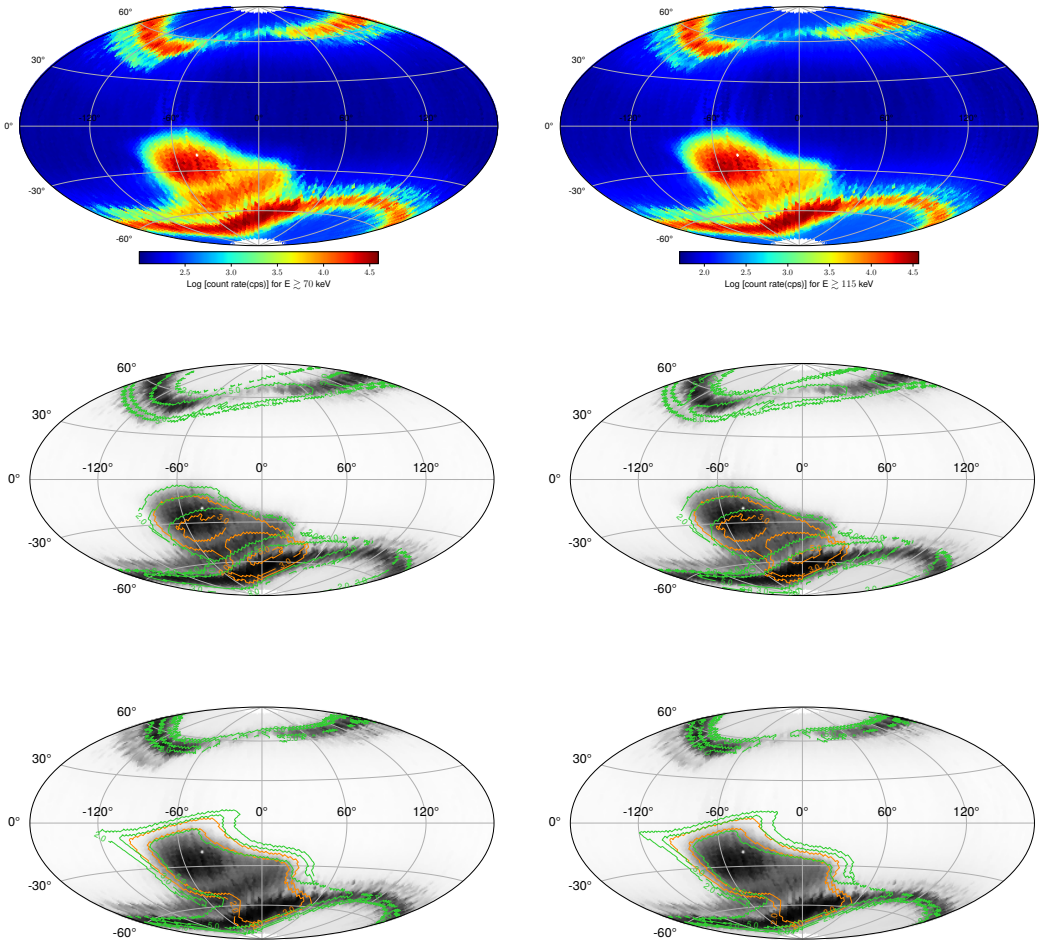

Figure 6.1: Measured background count rate by GRBAlpha at its initial altitude (550–525 km) and comparative analysis with AE8/AP8 and AE9/AP9 models across two energy bands: E $\gtrsim$ 70 keV (left column) and E $\gtrsim$ 115 keV (right column). Contours mark the particle flux of levels of $10^2, 10^3$, and 10^5 (particles $\mathrm{cm}^{-2}\mathrm{s}^{-1}$). *First row*: Median map of measured count rate. *Second row*: Median map of measured count rate with a comparison to AE8 (green contours) and AP8 (orange contours) during solar maximum. *Third row*: Median map of measured count rate with a comparison to AE9 (green contours) and AP9 (orange contours).

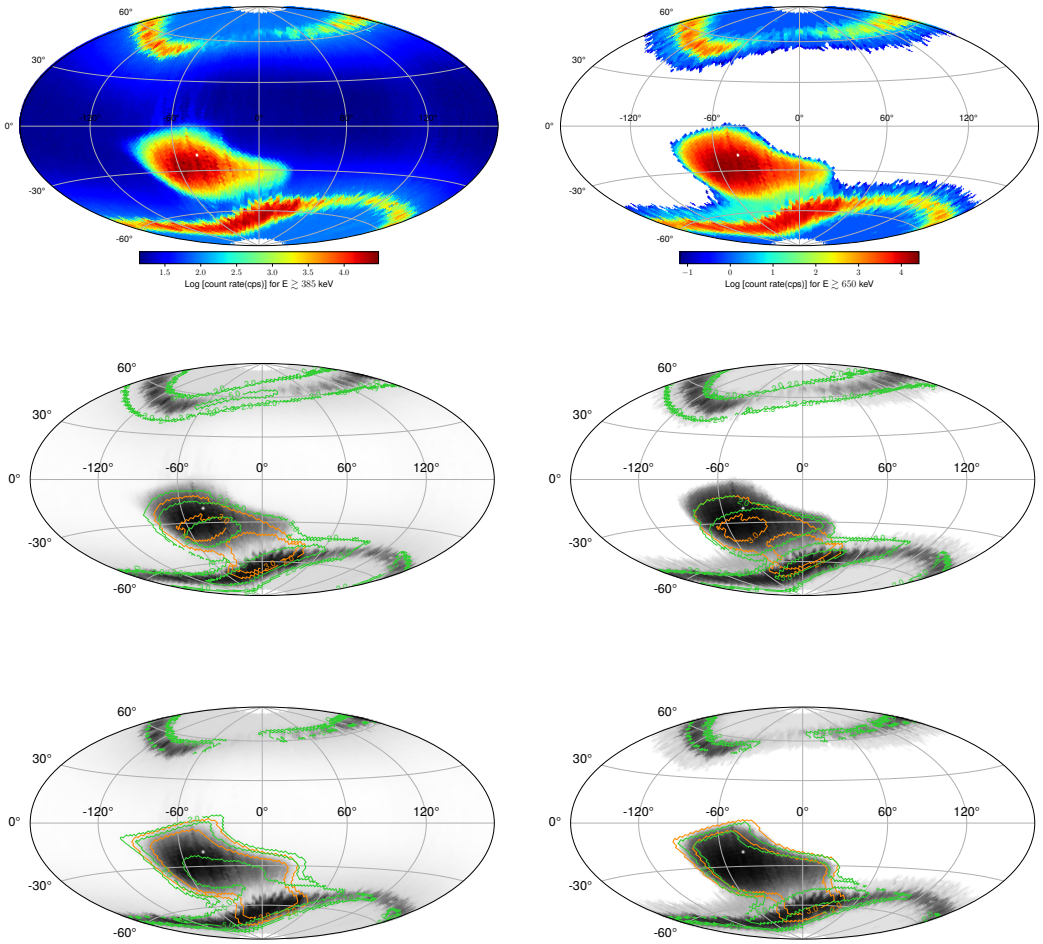

Figure 6.2: Measured background count rate by GRBAlpha at its initial altitude (550–525 km) and comparative analysis with AE8/AP8 and AE9/AP9 models across two energy bands: E $\gtrsim$ 385 keV (left column) and E $\gtrsim$ 650 keV (right column). Contours mark the particle flux of levels of $10^2, 10^3$, and 10^5 (particles $cm^{-2}s^{-1}$). *First row*: Median map of measured count rate. *Second row*: Median map of measured count rate with a comparison to AE8 (green contours) and AP8 (orange contours) during solar maximum. *Third row*: Median map of measured count rate with a comparison to AE9 (green contours) and AP9 (orange contours).

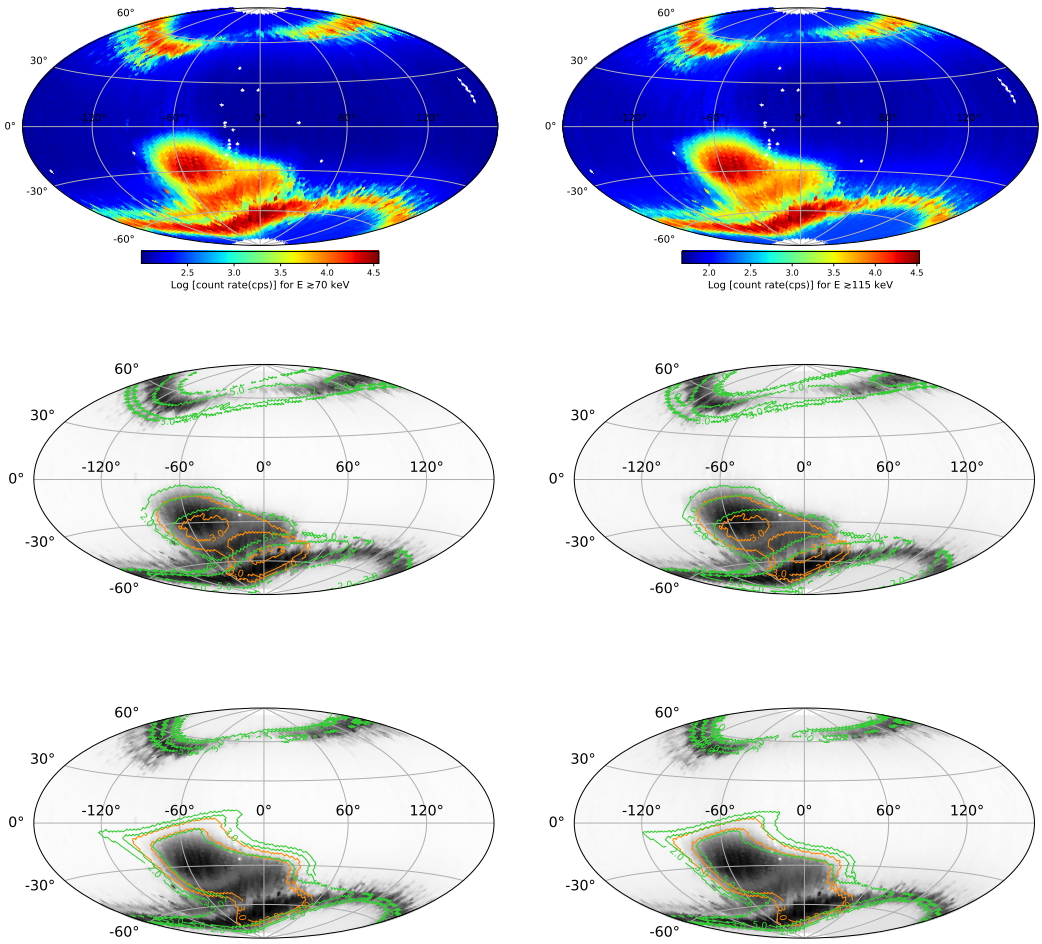

Figure 6.3: Measured background count rate by GRBAlpha at its lowered altitude (525–505 km) and comparative analysis with AE8/AP8 and AE9/AP9 models across two energy bands: E $\gtrsim$ 70 keV (left column) and E $\gtrsim$ 115 keV (right column). Contours mark the particle flux of levels of $10^2, 10^3$, and 10^5 (particles $\mathrm{cm}^{-2}\mathrm{s}^{-1}$). *First row*: Median map of measured count rate. *Second row*: Median map of measured count rate with a comparison to AE8 (green contours) and AP8 (orange contours) during solar maximum. *Third row*: Median map of measured count rate with a comparison to AE9 (green contours) and AP9 (orange contours).

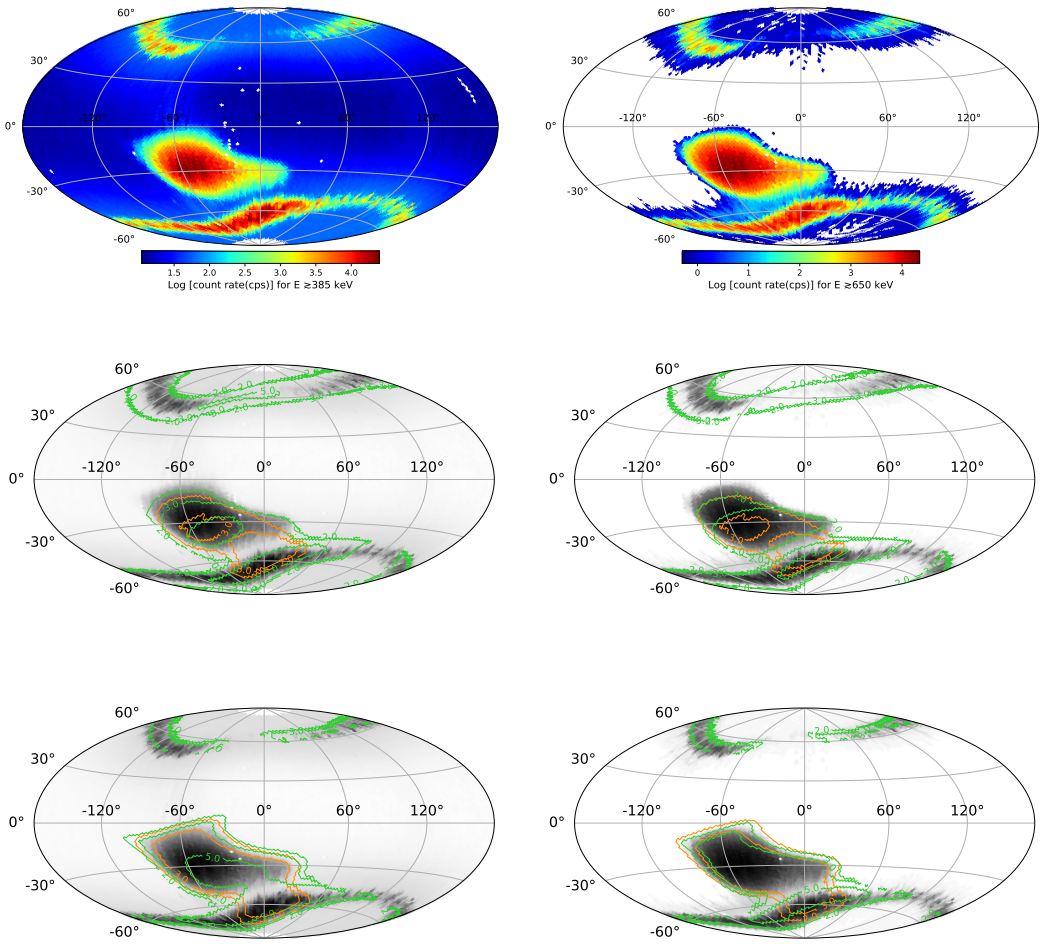

Figure 6.4: Measured background count rate by GRBAlpha at its lowered altitude (525–505 km) and comparative analysis with AE8/AP8 and AE9/AP9 models across two energy bands: E $\gtrsim$ 385 keV (left column) and E $\gtrsim$ 650 keV (right column). Contours mark the particle flux of levels of $10^2, 10^3$, and 10^5 (particles $cm^{-2}s^{-1}$). *First row*: Median map of measured count rate. *Second row*: Median map of measured count rate with a comparison to AE8 (green contours) and AP8 (orange contours) during solar maximum. *Third row*: Median map of measured count rate with a comparison to AE9 (green contours) and AP9 (orange contours).

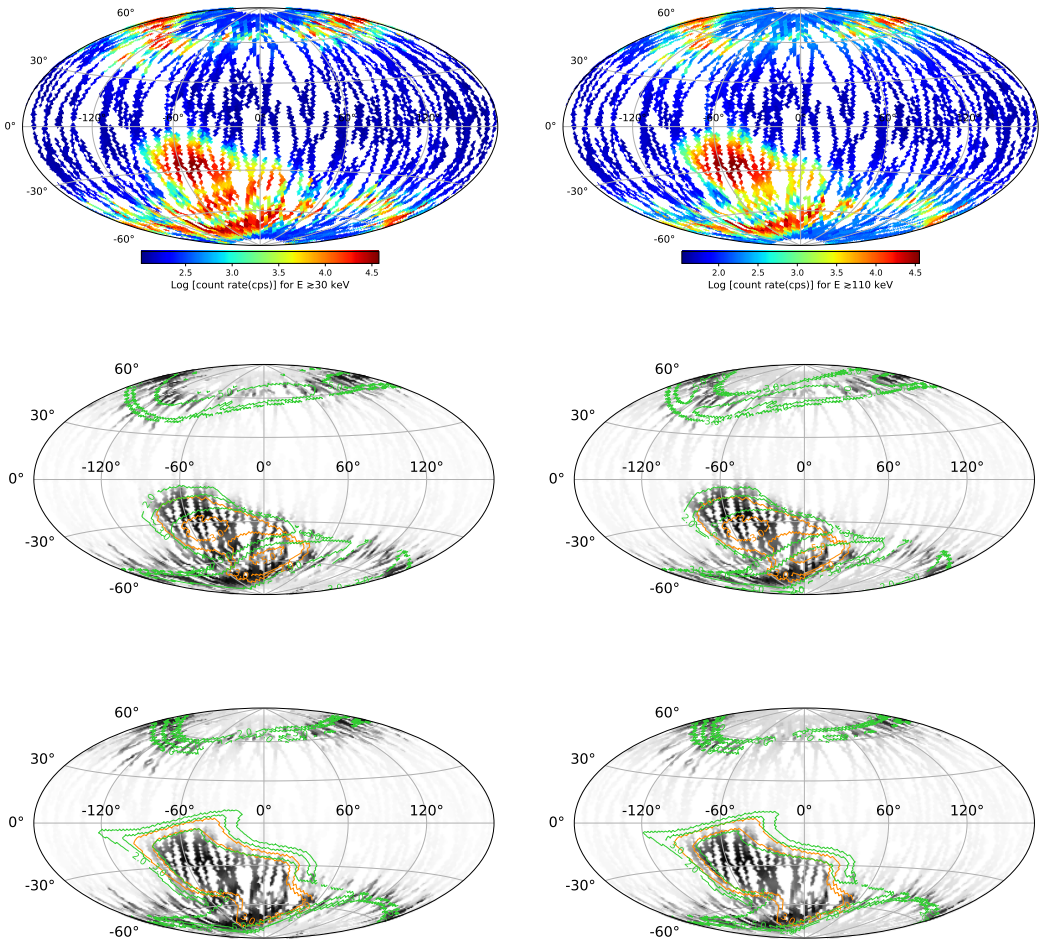

Figure 6.5: Measured background count rate by VZLUSAT-2 at altitudes (530–500 km) using no. 0 detector unit and comparative analysis with AE8/AP8 and AE9/AP9 models across two energy bands: E $\gtrsim$ 30 keV (left column) and E $\gtrsim$ 110 keV (right column). Contours mark the particle flux of levels of $10^2, 10^3$, and 10^5 (particles $\mathrm{cm}^{-2}\mathrm{s}^{-1}$). *First row*: Median map of measured count rate. *Second row*: Median map of measured count rate with a comparison to AE8 (green contours) and AP8 (orange contours) during solar maximum. *Third row*: Median map of measured count rate with a comparison to AE9 (green contours) and AP9 (orange contours).

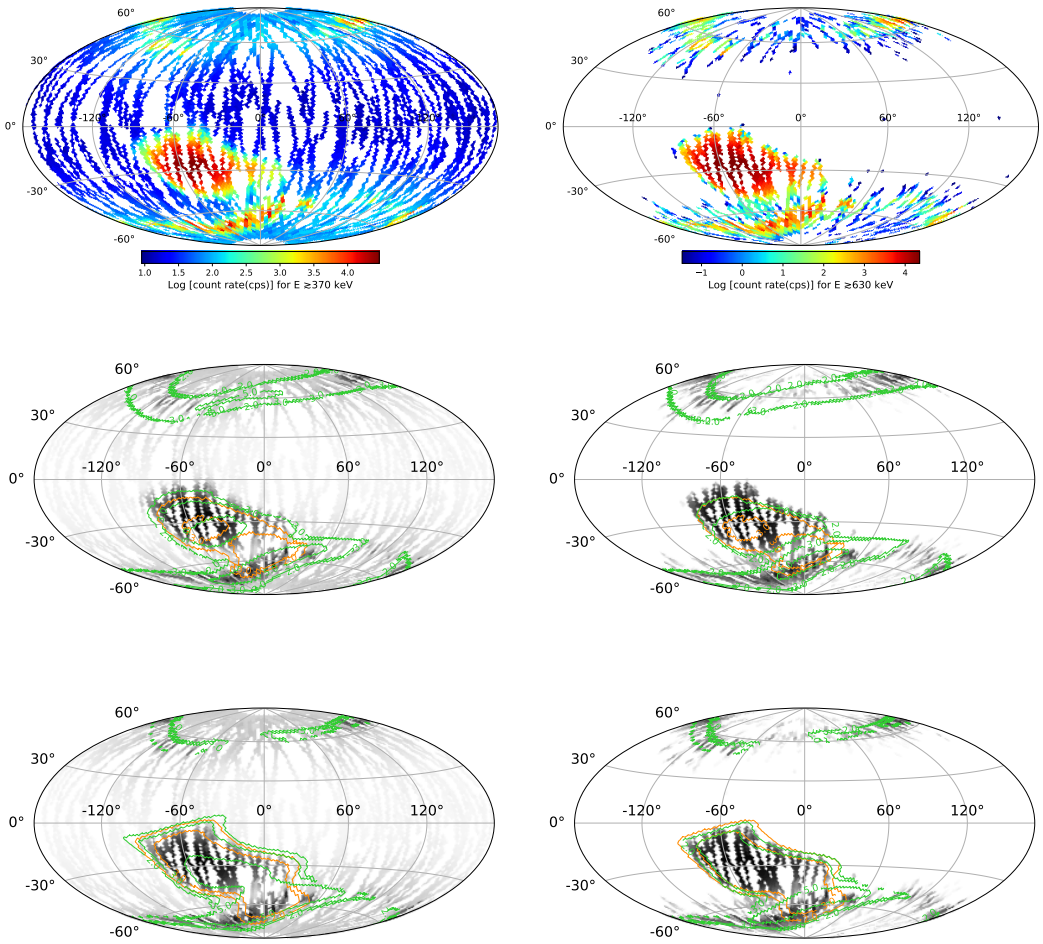

Figure 6.6: Measured background count rate by VZLUSAT-2 at altitudes (530–500 km) using no. 0 detector unit and comparative analysis with AE8/AP8 and AE9/AP9 models across two energy bands: E $\gtrsim$ 370 keV (left column) and E $\gtrsim$ 630 keV (right column). Contours mark the particle flux of levels of $10^2, 10^3$, and 10^5 (particles $\mathrm{cm}^{-2}\mathrm{s}^{-1}$). *First row*: Median map of measured count rate. *Second row*: Median map of measured count rate with a comparison to AE8 (green contours) and AP8 (orange contours) during solar maximum. *Third row*: Median map of measured count rate with a comparison to AE9 (green contours) and AP9 (orange contours).

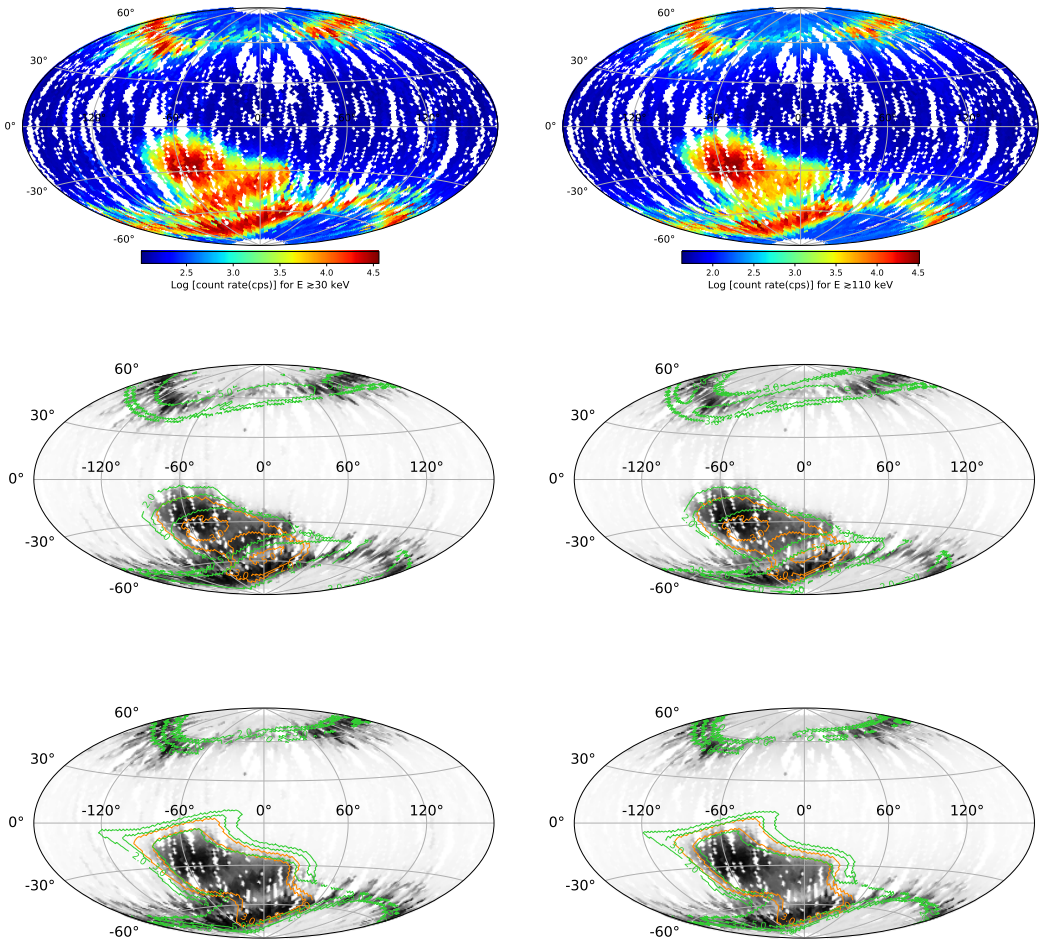

Figure 6.7: Measured background count rate by VZLUSAT-2 at altitudes (530–500 km) using no. 1 detector unit and comparative analysis with AE8/AP8 and AE9/AP9 models across two energy bands: E $\gtrsim$ 30 keV (left column) and E $\gtrsim$ 110 keV (right column). Contours mark the particle flux of levels of $10^2, 10^3$, and 10^5 (particles $\mathrm{cm}^{-2}\mathrm{s}^{-1}$). *First row*: Median map of measured count rate. *Second row*: Median map of measured count rate with a comparison to AE8 (green contours) and AP8 (orange contours) during solar maximum. *Third row*: Median map of measured count rate with a comparison to AE9 (green contours) and AP9 (orange contours).

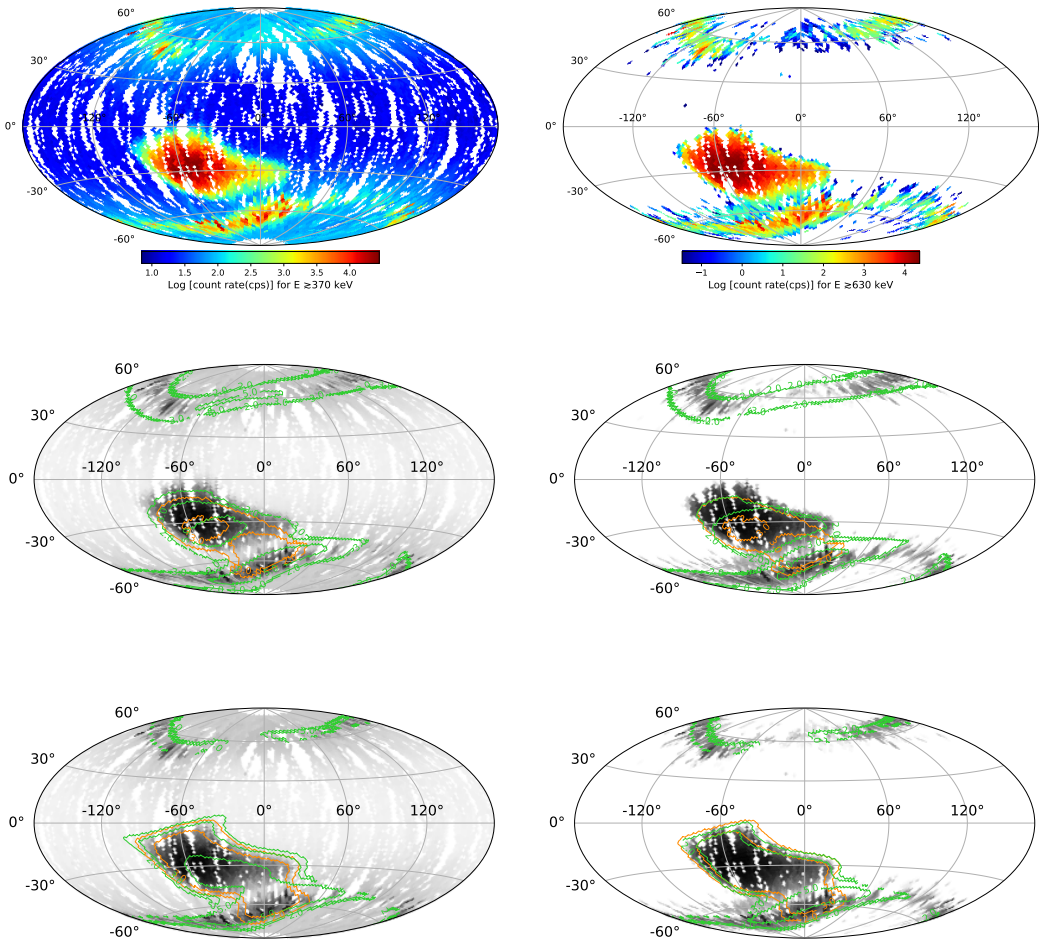

Figure 6.8: Measured background count rate by VZLUSAT-2 at altitudes (530–500 km) using no. 1 detector unit and comparative analysis with AE8/AP8 and AE9/AP9 models across two energy bands: E $\gtrsim$ 370 keV (left column) and E $\gtrsim$ 630 keV (right column). Contours mark the particle flux of levels of $10^2, 10^3$, and 10^5 (particles $\mathrm{cm}^{-2}\mathrm{s}^{-1}$). *First row*: Median map of measured count rate. *Second row*: Median map of measured count rate with a comparison to AE8 (green contours) and AP8 (orange contours) during solar maximum. *Third row*: Median map of measured count rate with a comparison to AE9 (green contours) and AP9 (orange contours).

6.2 EVALUATING THE TRIGGER ALGORITHM

6.2.1 *Exploring optimal threshold parameter*

The trigger algorithm relies on the threshold value k. This section describes our search for optimal k values across various trigger time windows and energy bands. The optimal k value should be balanced between being too high so it does not filter too many genuine detections and too low to avoid false triggering exceeding one per day. One of the assumptions is that even in areas with low background, higher values of k will be necessary to avoid false detections caused by the satellite's precession (Figure 6.9).

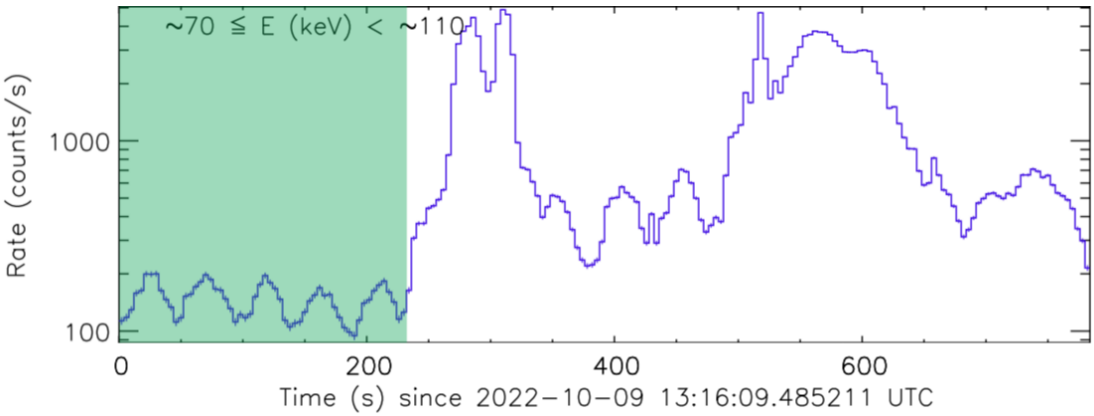

Figure 6.9: Raw count rate curve of GRB 221009A. The highlighted region shows a periodic signal in the light curve as the result of the CubeSat rotation/wobble. Figure from Konkoly, 2022.

Firstly, we created variability maps, shown in Figure 6.10, showing each pixel's coefficient of variability. The coefficient is the ratio of the standard deviation to the mean of count rate values. As Figure 6.10 shows, heightened variability regions coincide with the outer Van Allen Belt and the SAA (tip of the inner Van Allen Belt) with increased variability at the edges of these regions. This analysis also revealed that the final energy band (E>650 keV) is unusable due to the small number of counts in low background regions, so the mean value is less than one, resulting in high variability in those regions, so we did not use it.

One of our most important goals is that by running the trigger algorithm on a region of low background, we get no more than one false trigger per day. This goal is given by the correct choice of the parameter k, as shown in Figure 6.12. The first step is to define this low background region by some sophisticated method. We use only the first energy band (E $\gtrsim$ 70 keV) as an example of our analysis. Further steps are illustrated in Figure 6.11. Typically, a threshold value equivalent to 5–6 σ is chosen in many missions (Fenimore et al., 2003, Bhat et al., 2016 and Yamaoka et al., 2017). Thus, we begin by initially running the trigger algorithm across all GRBAlpha's data, omitting

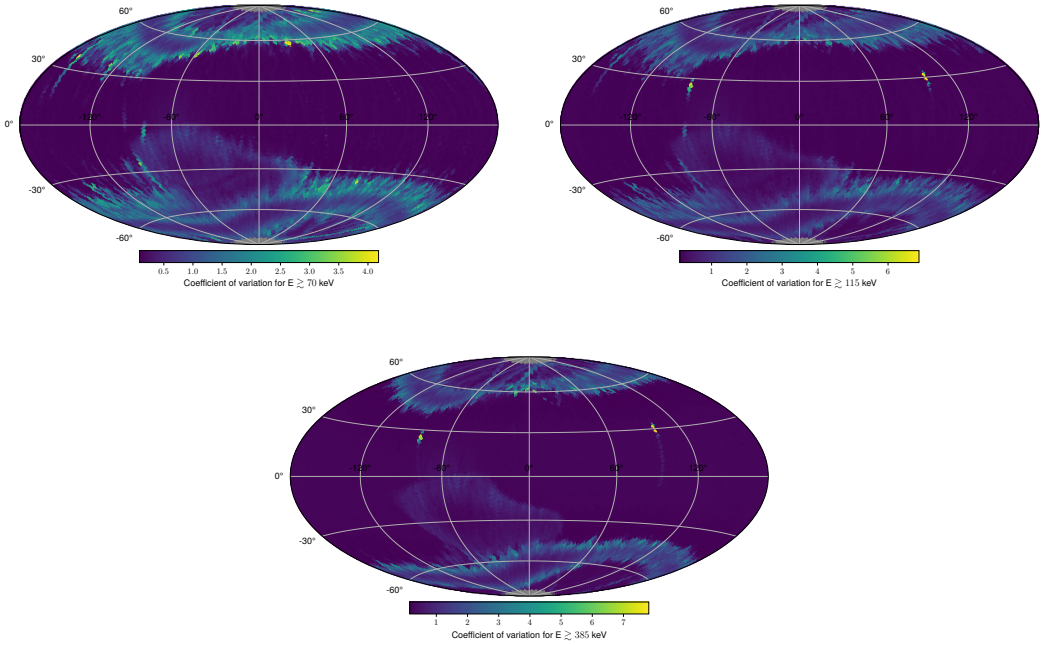

Figure 6.10: Variability of detected counts per second for GRBAlpha across three energy bands. Maps illustrate the coefficient of variation of the detected count rate for the respective energy band.

actual transients[1], with a lower threshold set as k=16 (corresponding to 4 σ). Then, we increased the threshold significantly to k=100 (equivalent to 10 σ), which generates a map mainly cleansed of false triggers in a region of low background while keeping most of those associated with high background regions. Therefore, threshold k=100 identifies the area needed for further exploration for optimal k values. We generated a mask using the clustering algorithm `HDBSCAN` (described in Section 5.2) to define this region, so the largest cluster with a low density of detections was identified. Within this region, we vary the set of k values across four trigger time windows:

$$\begin{aligned} \mathrm{k} &= \{16,\ 20.25,\ 25,\ 30.25,\ 36,\ 42.25,\ 49,\ 56.25,\ 64,\ 72.25,\ 81,\ 90.25,\ 100\} \\ (\mathrm{n}, \mathrm{N}) &= \{(1,32),\ (4,32),\ (16,32),\ (32,64)\}, \end{aligned} \tag{6.1}$$

giving a number of false triggers for various values of k. This allows us to observe if detected false triggers are satisfactorily randomly spread out in the resulting maps (no significant clustering near high background region borders), and it also gives us a number of false detections per day.

1 Transients detected by satellites GRBAlpha and VZLUSAT-2 can be found on web pages discussed in Appendix A.

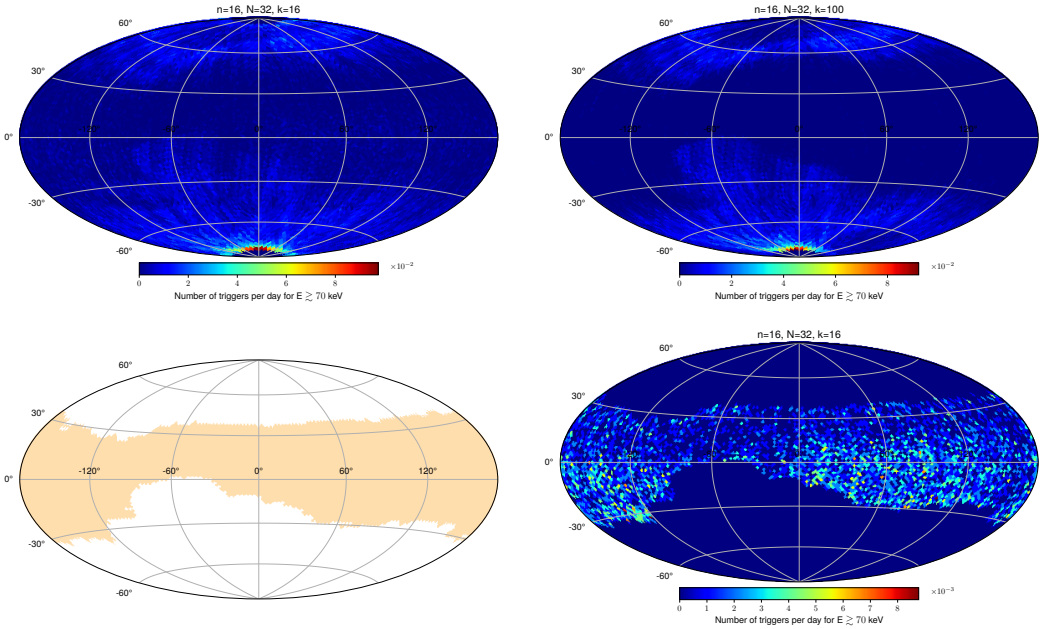

Figure 6.11: Illustration of trigger algorithm analysis and false trigger detection process. The trigger time window (16,32) is used as an example. *Top left*: Algorithm run on all data with a low threshold (k=16), showing widespread false triggers. *Top right*: Cleaned low background region resulting from the trigger algorithm run with a higher threshold (k=100). *Bottom left*: Mask generated using `HDBSCAN` clustering algorithm, highlighting the largest cluster of low detection density. *Bottom right*: An example of false triggers detected within this region.

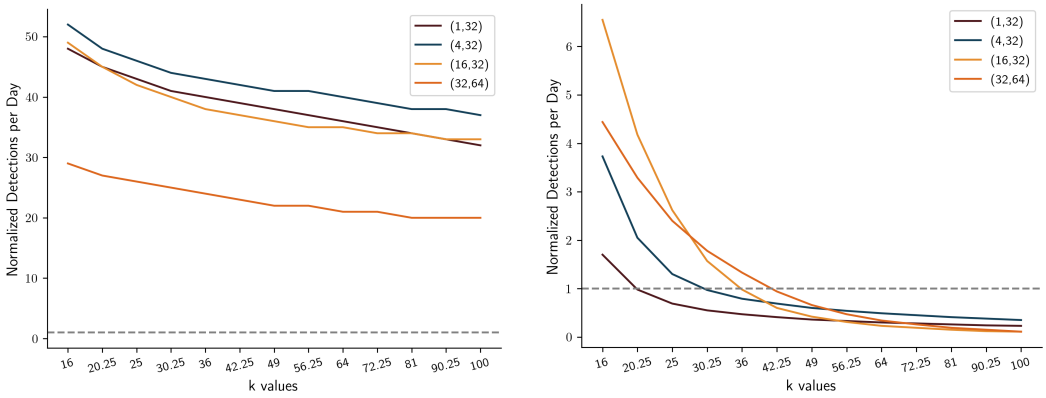

Figure 6.12: The graph shows the number of false triggers per day regarding increasing threshold parameter k for four different time windows within the E $\gtrsim$ 70 keV energy band. The goal is to achieve a false detection rate of less than one per day, indicated by the horizontal line. *Left*: Shows the number of false triggers per day when applying the trigger algorithm on the whole map. *Right*: Shows the number of false triggers per day when applying the trigger algorithm only on the low background region defined by the mask.

6.2.2 *Analysis with confirmed transients*

In this section, we are focusing only on confirmed unique transients. We created a dataset of 97 confirmed transients, each characterized by peak time—the time when the detected count rate reached its maximum value. Then, we specified a time interval of two minutes before and after each event's peak time. In the first row of Figure 6.13, we see the under-study dataset shown on the entire map and on the mask of the low-background region. We then applied the trigger algorithm to these intervals to see how many confirmed transients it found, shown in the second row of Figure 6.13.

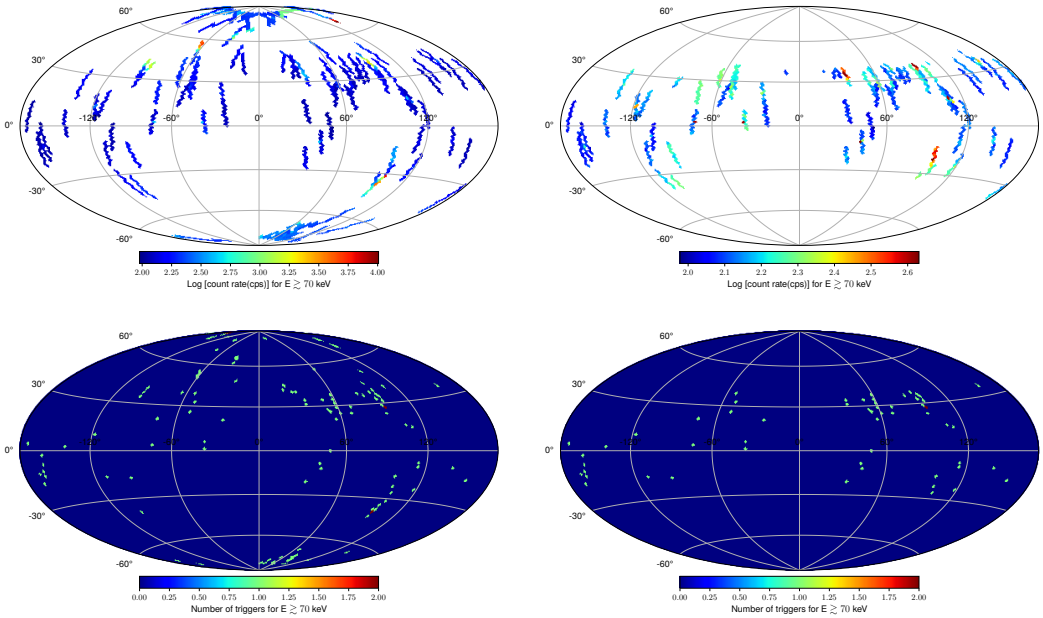

Figure 6.13: Performance of trigger algorithm with confirmed transients. *Top left*: The peak count rate of transients, with a two-minute interval before and after the peak. *Top right*: The same image focuses on regions with a low background. *Bottom left*: The number of triggers detected by the algorithm within the (1,32) time window. *Bottom right*: The same analysis within the low background region.

The inequality of the detected triggers using the algorithm (dark blue bars in Figure 6.14) with 97 actual transients is evident. For instance, at a value of k=16, we detected over 115 triggers despite only 97 unique transients. These arose from single transients where the count rate was increasing the way it fulfilled trigger conditions multiple times and produced multiple triggers.

Because of this higher number of detected triggers versus actual transients, we checked all detected triggers of E $\gtrsim$ 70 keV energy band and the (1,32) trigger time window. The number of triggers shown by dark blue bars corresponding with unique transients can be seen in Figure 6.14 shown by the green columns. It became appar-

ent that certain transients remained undetected by the trigger algorithm; for example, for k=16, only seventy triggers were unique transients. Moreover, the analysis showed reduced detected triggers when focusing only on low background regions, as shown by the yellow bars in Figure 6.14. This reduction accounts for over half of the total triggers detected across the map. Focusing only on the unique transient within the low background region, we can see another slight drop-down of detections, as shown by the orange bars in Figure 6.14. The percentage of unique triggers out of a total of 97 unique transients detected in the whole map and in the low background region only for different values of k are shown in Table 3.

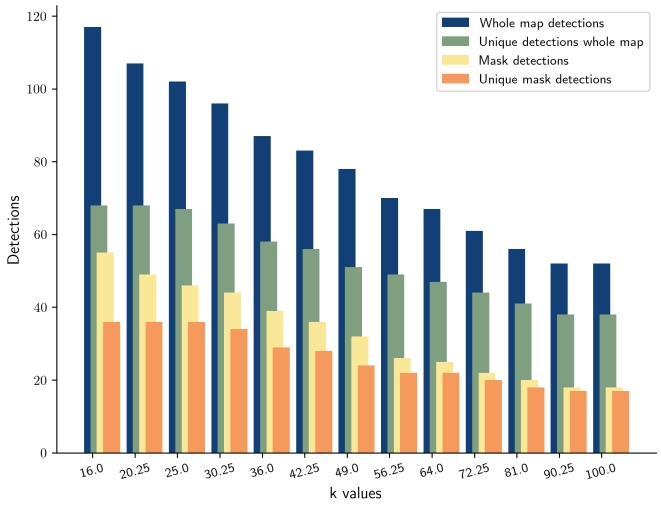

Figure 6.14: The graph shows the effectiveness of the trigger algorithm for the energy band E $\gtrsim$ 70 keV and time window (1,32) across different k values. The bar chart illustrates four specific results based on the detection of unique transients (97 in total). The dark blue bars represent the total number of detections collected on the entire map. The yellow bars show detections within regions of low background (mask detections). The green bars show the number of actual transients identified within the detections from the dark blue bars. The orange bars show the number of actual transients identified within the low background region only (mask detections).

Next, we wanted to study this reduced number of detections of confirmed transients. A manual verification of all triggers across various energy bands, time windows, and threshold parameter values was impossible. Therefore, we checked only the triggers for the E $\gtrsim$ 70 keV energy band for all four windows. This revealed cases where transients were detected using some of the other time windows, as shown in Figure 6.15. This analysis confirmed the necessity of all 4 types of trigger time windows working in parallel to capture as many different types of GRBs as possible. Furthermore, by a brief look, we also found some cases where transients undetected within the first energy band were detected in other energy bands.

k values	Whole map [%]	Mask [%]
16.00	70.10	37.11
20.25	70.10	37.11
25.00	69.07	37.11
30.25	64.95	35.05
36.00	59.79	29.90
42.25	57.73	28.87
49.00	52.58	24.74
56.25	50.52	22.68
64.00	48.45	22.68
72.25	45.36	20.62
81.00	42.27	18.56
90.25	39.18	17.53
100.00	39.18	17.53

Table 3: Percentage of uniquely detected transients for the case of the whole map or low background region (mask) out of a total of 97 transients.

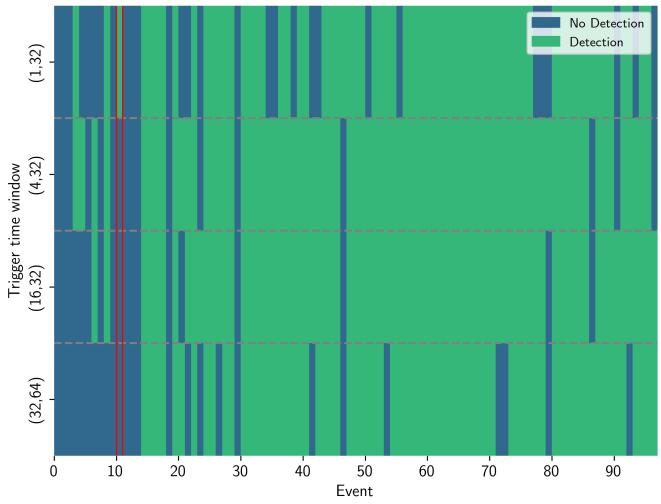

Figure 6.15: The image shows the detection status of 97 confirmed transients across four trigger time windows for the E $\gtrsim$ 70 keV energy band. Each event is marked along the x-axis, while the y-axis corresponds to the different time windows. Blue indicates no detection, while green denotes detection by the respective window. The example highlighted by the red box shows a transient detected only by the (1,32) time window and remains undetected by other windows.

6.2.3 *Trigger algorithm across three energy bands*

We extended our previous analysis to include various combinations of energy bands, threshold parameter values, and trigger time windows. First, we looked at the effectiveness of the trigger algorithm in all three energy bands. First of all, we checked whether specific transients (total 97) were detected in an individual energy band regardless of the particular trigger time window and k value. Figure 6.16 shows that the first energy band, E $\gtrsim$ 70 keV, is the most effective, with the most captured detections. Still, in some cases, the remaining two energy bands complement the first energy band and thus increase the number of detected transients. Next, we looked closer at the cases when the trigger algorithm did not detect a particular transient in any energy band. Figure 6.17 shows light curves where the transient was undetected using the trigger algorithm. The red line shows the peak time of the undetected transient. The transient in all three energy bands almost or entirely merges with the background. The reason it was found in GRBAlpha's data (when we looked for it based on detections by other satellites) was that different energy band ranges were used to capture it (see GRB 220915A on the web). For comparison, Figure 6.18 shows a case (GRB 230911D) where one specific transient was found in the light curves of all three energy bands.

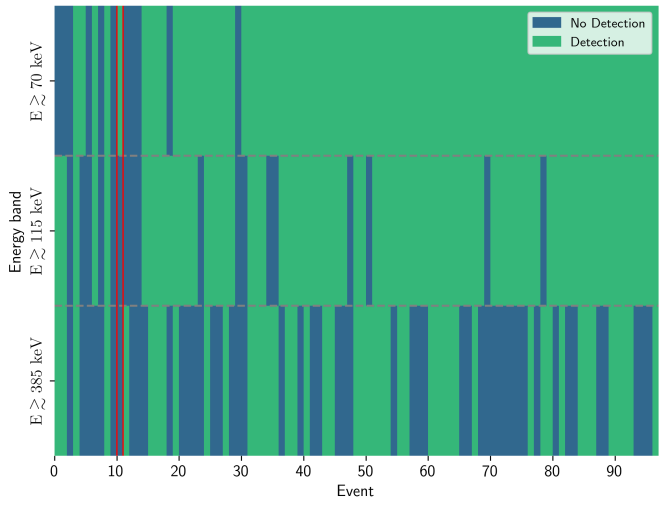

Figure 6.16: The image shows the detection status of 97 confirmed transients across three energy bands regardless of the specific trigger time window and the value of k. Each event is marked along the x-axis, while the y-axis corresponds to the different energy bands. Blue indicates no detection, while green denotes detection by the respective window. The example highlighted by the red box shows a transient detected only by the E $\gtrsim$ 70 keV energy band and remains undetected by other energy bands.

The area in which we recommend turning off the trigger algorithm can be determined in two ways. The first way is to leave a specific mask for each combination of the trigger time window and energy band separately. For some combinations of

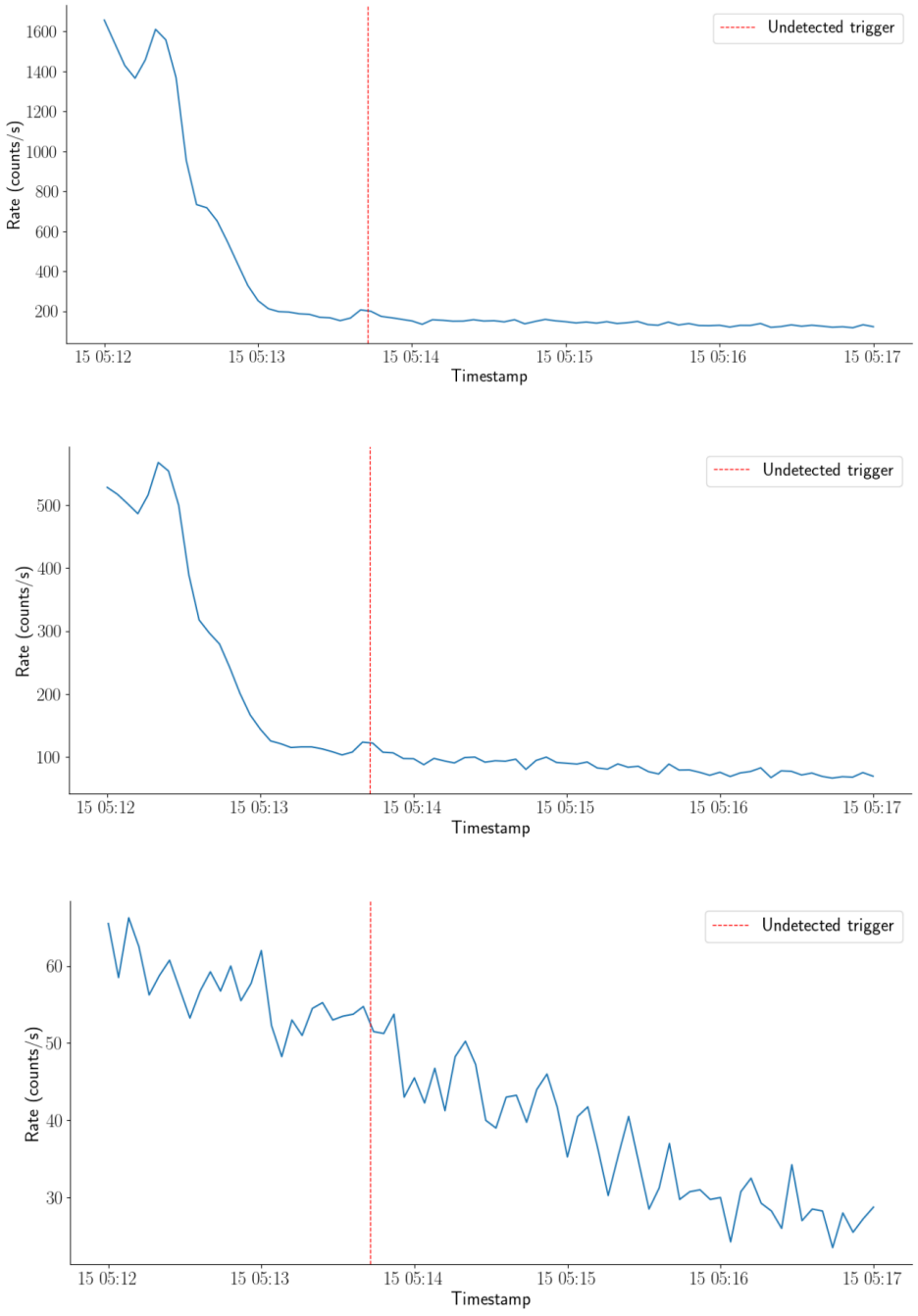

Figure 6.17: The light curves of the undetected transient GRB 220915A for three bands, with the peak time marked by a red dashed line. The top image represents band E $\gtrsim$ 70 keV, the middle image represents band E $\gtrsim$ 115 keV, and the bottom image represents band E $\gtrsim$ 385 keV.

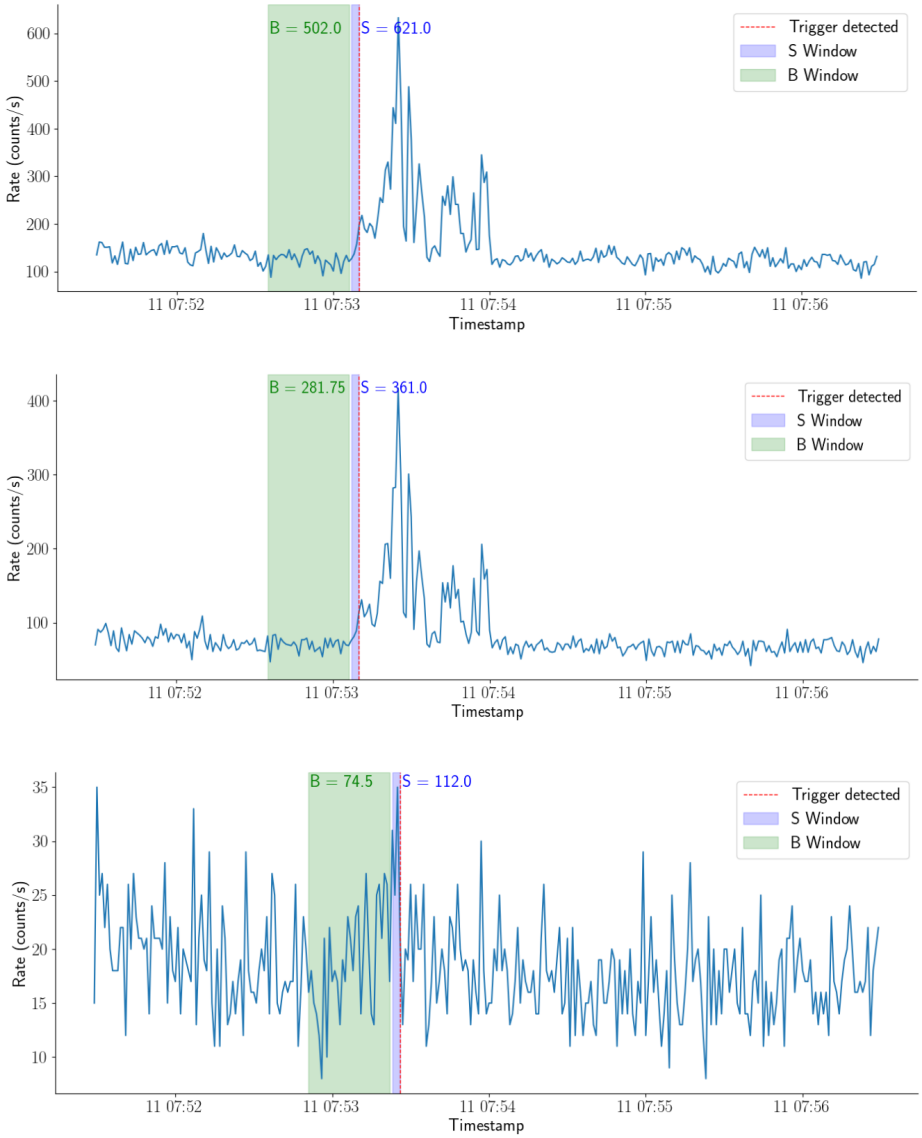

Figure 6.18: The light curves of the detected transient GRB 230911D for three bands, with the time of the trigger marked by a red dashed line. The top image represents band E $\gtrsim$ 70 keV, the middle image represents band E $\gtrsim$ 115 keV, and the bottom image represents band E $\gtrsim$ 385 keV. The setting for the trigger time window was (4, 32) with a value of k=16.

energy band and trigger time window, such a method can give us a bigger region of low background and, therefore, a larger number of potential detections. Figure 6.19 illustrates the behaviour of particular trigger time windows at specific energies and corresponding masks. The recommended values of the parameter k for this scenario are given in Table 4 at left. Another approach is to create a universal mask for all

combinations of energy bands and trigger time windows, as shown in Figure 6.20. The mask was created by combining all the maps for all combinations of the energy band with trigger time windows, setting the threshold parameter k=100. The recommended k parameter values for this type of mask are provided in Table 4. We expected that a higher threshold value than the common value of around 5 σ would be required because of the rotational motion of GRBAlpha and the associated background fluctuations. Surprisingly, our findings deviated from initial expectations. Lower threshold values ranging from 4–6 σ were sufficient across most energy bands and trigger time windows. The trigger time window (32,64) was more sensitive to satellite precision. Therefore, a higher threshold is required to detect up to one false trigger per day. The analysis also showed the potential of using masks adjusted to individual energy bands and trigger time windows for regions of heightened background. False triggers were effectively reduced by selectively turning off the trigger algorithm during these regions.

	(1,32)	(4,32)	(16,32)	(32,64)
E $\gtrsim$ 70 keV	20.25	30.25	36	42.25
E $\gtrsim$ 115 keV	16	20.25	30.25	36
E $\gtrsim$ 385 keV	20.25	20.25	25	72.25

	(1,32)	(4,32)	(16,32)	(32,64)
E $\gtrsim$ 70 keV	20.25	25	42.25	64
E $\gtrsim$ 115 keV	16	16	25	49
E $\gtrsim$ 385 keV	16	16	25	42.25

Table 4: The table presents the recommended threshold parameters k for three energy bands and four trigger time windows. *Left*: Threshold values for the scenario, with more masks unique for each combination of energy band and trigger time window. *Right*: Threshold values for the scenario with one universal mask.

Using more advanced algorithms can reduce the number of false triggers. One such algorithm was developed for HETE-2 or Swift/BAT, which involved using two background windows—one before and one behind the foreground window. This enabled the linear interpolation and, thus, estimation of the background in the foreground window. This approach is particularly important for effectively removing false triggers caused by the rising background trend (Fenimore and Galassi, 2001, Tavenner et al., 2003).

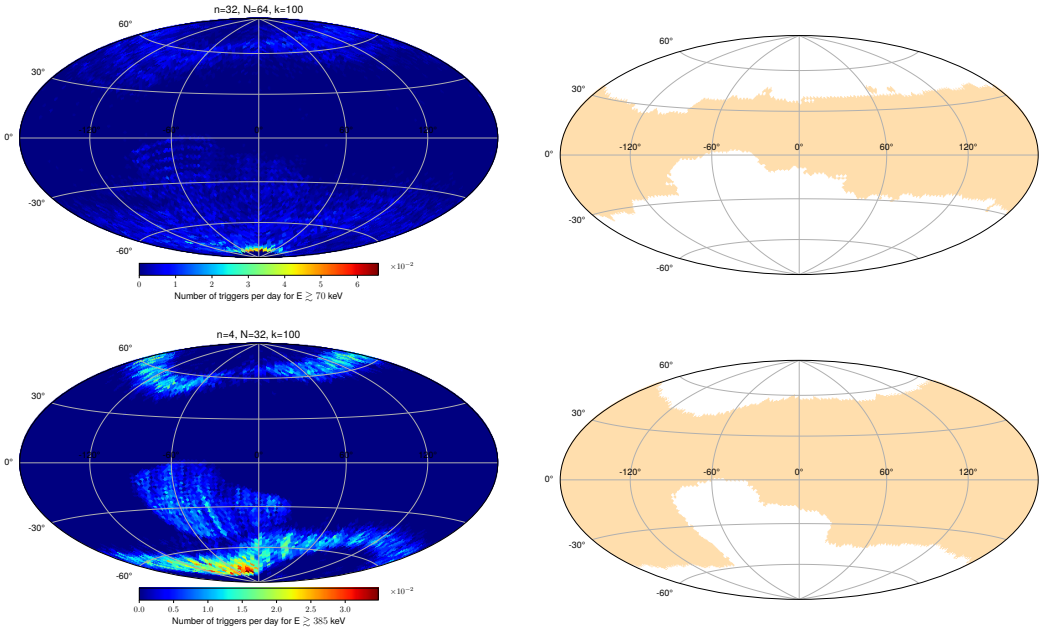

Figure 6.19: Comparison of trigger algorithm performance for different combinations of energy band and trigger time window. *First row*: Represent triggers for energy band E $\gtrsim$ 70 keV and trigger time window (32,64) (*left*), and corresponding mask of low background region (*right*). *Second row*: Represent triggers for energy band E $\gtrsim$ 385 keV and trigger time window (4,32) (*left*), and corresponding mask of low background region (*right*).

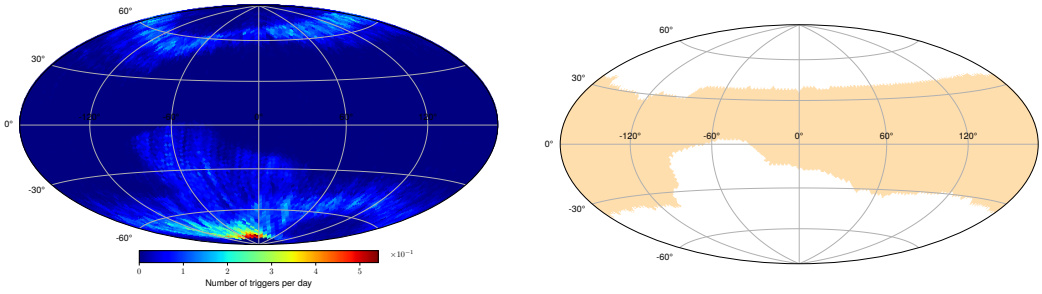

Figure 6.20: Universal map for all combinations of energy bands and trigger time windows (*left*), and corresponding mask of low background region (*right*).

CONCLUSION

In the first part of our work, we did a comparative analysis of models of captured particles AE8, AP8, AE9, and AP9 with measured data from GRBAlpha and VZLUSAT-2 satellites. We focused on investigating the spatial distribution of the Van Allen belts and the South Atlantic anomaly on maps created using the `HEALPix` tool. When examining the maps, we distinguished between two different GRBAlpha altitudes – initial and reduced, and between two VZLUSAT-2 detectors. We also analysed data from four different energy bands for each dataset.

In Chapter 3, we focused on modelling the map for both satellites and processing the map of measured data with the `HEALPix` tool implemented in the Python package Healpy. In the Section 6.1, we focused on comparative analysis. First, we noticed that all the maps of the measured data are almost identical. This is probably because both satellite detectors measured at approximately the same time at similar altitudes and with approximately the same orbit. We see changes only in energy bands; we measure lower particle fluxes at higher band energies.

Furthermore, we found that while the models generally capture the overall shape of the Van Allen Belt and South Atlantic Anomaly regions, they deviate mainly in predicting peak flows. Models AE8 and AP8 described the data better in the lower energy bands, providing a reasonably accurate prediction of the overall shape of these areas. However, the estimate of the peak flows was shifted compared to the measured data. On the other hand, the AE9 and AP9 models provided a better description of the overall shape of these areas in the two higher energy bands but overestimated the fluxes; thereby, the peak fluxes structures in these areas were lost. This can be seen in 6.1, 6.2, 6.3, 6.4 in Section 6.1.1 for GRBAlpha and in Figures 6.5, 6.6, 6.7, 6.8 in Section 6.1.2 for VZLUSAT-2.

In the second part of this work, we used the background measured by the GRBAlpha satellite to test the effectiveness of the trigger algorithm. The goal was to choose the optimal threshold parameter so that the number of false triggers does not exceed one per day while still capturing a sufficient number of actual transients.

This part of the work confirmed that, for this type of trigger algorithm, the trigger algorithm should be working only in areas with low background, as seen in Graph 6.12.

In Section 6.2.2, we focused only on confirmed transients. The effectiveness of the trigger algorithm in areas with low background compared to the effectiveness of the whole map for a single time window can be seen in Figure 6.14 and Table 3.

In Graph 6.15, we see that even if some transients were not picked up by one trigger time window, they could be found by any of the remaining three, confirming the importance of using all four windows in parallel.

The resulting optimal threshold values for all combinations of the four trigger time windows and three energy bands are shown in Table 4.

Using this trigger algorithm, especially in areas with low background, could significantly improve future CubeSat missions aimed at gamma-ray burst detection. In contrast to the current approach of downloading data from GRBAlpha only after transients have been detected by other satellites, implementing this trigger algorithm within a larger group of CubeSats could ensure that these CubeSats can detect transients not previously detected by other satellites. This could provide even more GRB data and, thus, contribute to a better understanding of the origin of GRBs.

Part IV

APPENDIX

APPENDIX A

During our work, we have been uploading detections of satellites on the websites for GRBAlpha and VZLUSAT-2. Figure A.1 shows a sample of the site.

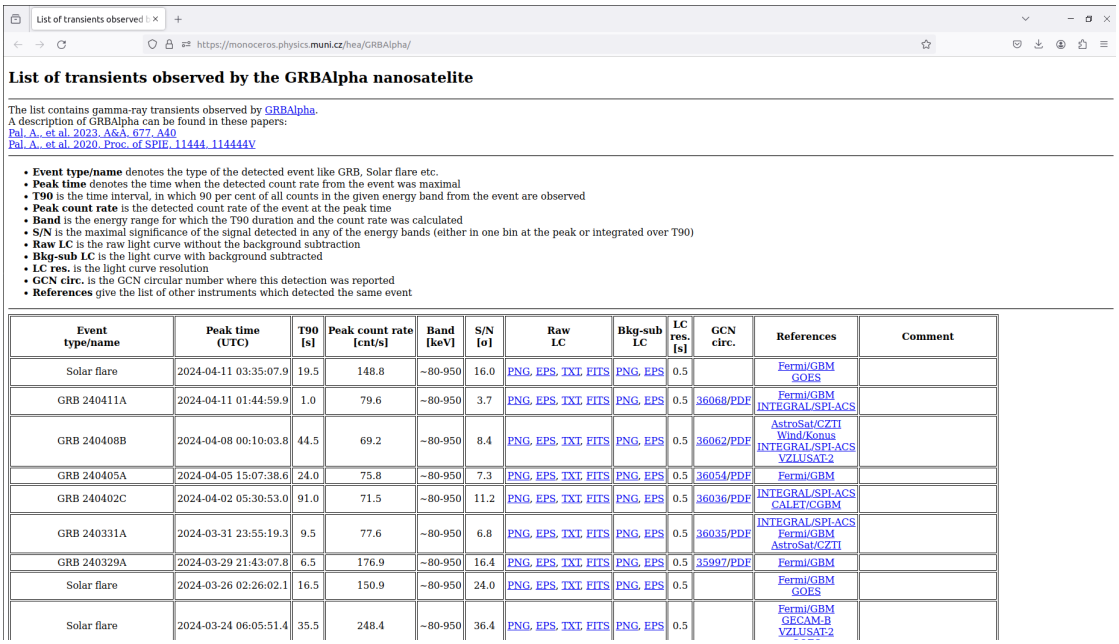

List of transients observed | https://monoceros.physics.muni.cz/hea/GRBAlpha/

List of transients observed by the GRBAlpha nanosatelite

The list contains gamma-ray transients observed by GRBAlpha.
A description of GRBAlpha can be found in these papers:
Pal, A., et al. 2023, A&A, 677, A40
Pal, A., et al. 2020, Proc. of SPIE, 11444, 114444V

- **Event type/name** denotes the type of the detected event like GRB, Solar flare etc.
- **Peak time** denotes the time when the detected count rate from the event was maximal
- **T90** is the time interval, in which 90 per cent of all counts in the given energy band from the event are observed
- **Peak count rate** is the detected count rate of the event at the peak time
- **Band** is the energy range for which the T90 duration and the count rate was calculated
- **S/N** is the maximal significance of the signal detected in any of the energy bands (either in one bin at the peak or integrated over T90)
- **Raw LC** is the raw light curve without the background subtraction
- **Bkg-sub LC** is the light curve with background subtracted
- **LC res.** is the light curve resolution
- **GCN circ.** is the GCN circular number where this detection was reported
- **References** give the list of other instruments which detected the same event

Event type/name	Peak time (UTC)	T90 [s]	Peak count rate [cnt/s]	Band [keV]	S/N [σ]	Raw LC	Bkg-sub LC	LC res. [s]	GCN circ.	References	Comment
Solar flare	2024-04-11 03:35:07.9	19.5	148.8	~80-950	16.0	PNG, EPS, TXT, FITS	PNG, EPS	0.5		Fermi/GBM GOES	
GRB 240411A	2024-04-11 01:44:59.9	1.0	79.6	~80-950	3.7	PNG, EPS, TXT, FITS	PNG, EPS	0.5	36068/PDF	Fermi/GBM INTEGRAL/SPI-ACS	
GRB 240408B	2024-04-08 00:10:03.8	44.5	69.2	~80-950	8.4	PNG, EPS, TXT, FITS	PNG, EPS	0.5	36062/PDF	AstroSat/CZTI Wind/Konus INTEGRAL/SPI-ACS VZLUSAT-2	
GRB 240405A	2024-04-05 15:07:38.6	24.0	75.8	~80-950	7.3	PNG, EPS, TXT, FITS	PNG, EPS	0.5	36054/PDF	Fermi/GBM	
GRB 240402C	2024-04-02 05:30:53.0	91.0	71.5	~80-950	11.2	PNG, EPS, TXT, FITS	PNG, EPS	0.5	36036/PDF	INTEGRAL/SPI-ACS CALET/CGBM	
GRB 240331A	2024-03-31 23:55:19.3	9.5	77.6	~80-950	6.8	PNG, EPS, TXT, FITS	PNG, EPS	0.5	36035/PDF	INTEGRAL/SPI-ACS Fermi/GBM AstroSat/CZTI	
GRB 240329A	2024-03-29 21:43:07.8	6.5	176.9	~80-950	16.4	PNG, EPS, TXT, FITS	PNG, EPS	0.5	35997/PDF	Fermi/GBM	
Solar flare	2024-03-26 02:26:02.1	16.5	150.9	~80-950	24.0	PNG, EPS, TXT, FITS	PNG, EPS	0.5		Fermi/GBM GOES	
Solar flare	2024-03-24 06:05:51.4	35.5	248.4	~80-950	36.4	PNG, EPS, TXT, FITS	PNG, EPS	0.5		Fermi/GBM GECAM-B VZLUSAT-2	

Figure A.1: The list of transients detected by GRBAlpha.

BIBLIOGRAPHY

[1]S. Agostinelli et al., "GEANT4: A simulation toolkit," Nucl. Instrum. Meth. **A506**, 250–303 (2003).

[2]J. A. van Allen, "Spatial distribution and time decay of the intensities of geomagnetically trapped electrons from the high altitude nuclear burst of july 1962," in Radiation trapped in the earth's magnetic field, edited by B. M. McCormac (1966), pp. 575–592.

[3]D. N. Baker, P. R. Higbie, R. D. Belian, and E. W. Hones Jr., "Do jovian electrons influence the terrestrial outer radiation zone?" Geophysical Research Letters **6**, 531–534 (1979).

[4]D. Baker, P. Erickson, J. Fennell, J. Foster, A. Jaynes, and P. Verronen, "Space weather effects in the earth's radiation belts," Space Science Reviews **214**, 10.1007/s11214-017-0452-7 (2017).

[5]D. N. Baker, "How to cope with space weather," Science **297**, 1486–1487 (2002).

[6]P. Berba, *Hdbscan*, [Accessed: 20.4.2024], (2021) https://pberba.github.io/stats/2020/01/17/hdbscan/.

[7]P. N. Bhat, C. A. Meegan, A. von Kienlin, et al., "The third fermi gbm gamma-ray burst catalog: the first six years," The Astrophysical Journal Supplement Series **223**, 28 (2016).

[8]J. C. Cain, "Models of the earth's magnetic field.," pp 7-25 of Radiation Trapped in the Earth's Magnetic Field. McCormac, Billy M. (ed.). New York, Gordon and Breach Science Publishers, 1966. (1967).

[9]X. Cui, Q. Zhenxian, X. Chen, Z. Zhang, et al., "Gpr-based automatic identification of root zones of influence using hdbscan," Remote Sensing **13**, 10.3390/rs13061227 (2021).

[10]J. Cummings, A. Cummings, R. Mewaldt, R. Selesnick, E. Stone, T. Von Rosenvinge, and J. Blake, "Sampex measurements of heavy ions trapped in the magnetosphere," IEEE Transactions on Nuclear Science **40**, 1458–1462 (1993).

[11]M. Dafčíková, *Modeling the low earth orbit particle background of grb alpha using space weather data [online]*, Bachelor thesis, SUPERVISOR : Jean-Paul Bernhard Riffald Souza Breuer, 2022.

[12]ESA, *South atlantic anomaly*, [Accessed: 24.4.2024], (2024) https://www.esa.int/ESA_Multimedia/Images/2007/03/Earth_radiation_belts_with_the_South_Atlantic_Anomaly_indicated.

[13]E. E. Fenimore and M. Galassi, "The HETE Triggering Algorithm," in Gamma-ray bursts in the afterglow era, edited by E. Costa, F. Frontera, and J. Hjorth (Jan. 2001), p. 393.

[14]E. E. Fenimore, D. Palmer, Galassi, et al., "The Trigger Algorithm for the Burst Alert Telescope on Swift," AIP Conference Proceedings **662**, 491–493 (2003).

[15]J. F. Fennell, S. G. Claudepierre, J. B. Blake, O'Brien, et al., "Van allen probes show that the inner radiation zone contains no mev electrons: ect/mageis data," Geophysical Research Letters **42**, 1283–1289 (2015).

[16]S. Fung, "Recent development in the nasa trapped radiation models," Radiation Belts: Models and Standards **97**, 79–91 (1996).

[17]GRBAlpha, [Accessed: 20.4.2024], (2024) https://grbalpha.konkoly.hu/.

[18]G. Ginet, T. O'Brien, S. Huston, W. Johnston, et al., "Ae9, ap9 and spm: new models for specifying the trapped energetic particle and space plasma environment," Space Science Reviews **179**, 10.1007/s11214-013-9964y (2013).

[19]K. M. Gorski, E. Hivon, A. J. Banday, B. D. Wandelt, F. K. Hansen, M. Reinecke, and M. Bartelmann, "Healpix: a framework for high-resolution discretization and fast analysis of data distributed on the sphere," The Astrophysical Journal **622**, 759–771 (2005).

[20]S. Jeong, M. I. Panasyuk, V. Reglero, P. Connell, M. B. Kim, et al., "UBAT of UFFO/Lomonosov: The X-Ray Space Telescope to Observe Early Photons from Gamma-Ray Bursts," **214**, 16, 16 (2018).

[21]W. Johnston, T. O'Brien, G. Ginet, S. Huston, T. Guild, and J. Fennelly, "Ae9/ap9/spm: new models for radiation belt and space plasma specification," in , Vol. 9085 (June 2014), p. 908508.

[22]I. Jun and H. B. Garrett, "Comparison of high-energy trapped particle environments at the earth and jupiter," Radiation Protection Dosimetry **116**, 50–54 (2005).

[23]D. T. Kelso, *Celestrak*, [Accessed: 24.4.2024], (2024) https://celestrak.org/.

[24]B. Klecker, M. C. McNab, J. B. Blake, D. C. Hamilton, et al., "Charge State of Anomalous Cosmic-Ray Nitrogen, Oxygen, and Neon: SAMPEX Observations," **442**, L69 (1995).

[25]G. F. Knoll, *Radiation detection and measurement; 4th ed.* (Wiley, New York, NY, 2010).

[26]Konkoly, [Accessed: 20.4.2024], (2022) https://grbalpha.konkoly.hu/static/share/GRB221009A_GCN_GRBAlpha.pdf.

[27]S. A. Leland McInnes John Healy, *Hdbscan*, [Accessed: 20.4.2024], (2016) https://hdbscan.readthedocs.io/en/latest/how_hdbscan_works.html.

[28]X. Li, R. S. Selesnick, D. N. Baker, A. N. Jaynes, Kanekal, et al., "Upper limit on the inner radiation belt mev electron intensity," Journal of Geophysical Research: Space Physics **120**, 1215–1228 (2015).

[29]K. R. Lorentzen, J. E. Mazur, M. D. Looper, J. F. Fennell, and J. B. Blake, "Multi-satellite observations of mev ion injections during storms," Journal of Geophysical Research: Space Physics **107**, SMP 7–1–SMP 7–11 (2002).

[30]V. Maget, S. Bourdarie, D. Lazaro, D. Boscher, G. Rolland, R. Ecoffet, and E. Lorfèvre, "Unfolding jason-2/icare-ng high-energy particles measurements using a singular value decomposition approach," IEEE Transactions on Nuclear Science **61**, 1687–1694 (2014).

[31]L. M. Martinez, *Analysis of leo radiation environment and its effects on spacecraft's critical electronic devices [online]*, Master thesis, 2011.

[32]L. McInnes, J. Healy, and S. Astels, "Hdbscan: hierarchical density based clustering," The Journal of Open Source Software **2**, 205 (2017).

[33]S. Motalebi, *Healpix and healpy – with examples*, Feb. 2020.

[34]Motions, [Accessed: 20.4.2024], (2024) https://earthscience.stackexchange.com/questions/22911/why-do-electrons-drift-eastwards-in-the-van-allen-belts.

[35]L. Métrailler, *Unbuckling the van allen belts: from discovery to modern models (presentation)*, [Accessed: 24.4.2024], (2019) https://www.esa.int/ESA_Multimedia/Images/2007/03/Earth_radiation_belts_with_the_South_Atlantic_Anomaly_indicated.

[36]G. W. Na, S. Ahmad, P. Barrillon, S. Brandt, C. Budtz-Jørgensen, et al., "The readout system and the trigger algorithm implementation for the UFFO Pathfinder," in Space telescopes and instrumentation 2012: ultraviolet to gamma ray, Vol. 8443, edited by T. Takahashi, S. S. Murray, and J.-W. A. den Herder, Society of Photo-Optical Instrumentation Engineers (SPIE) Conference Series (Sept. 2012), 84432T.

[37]SPENVIS, *Trapped particle radiation models*, [Accessed: 24.4.2024], (2018) https://www.spenvis.oma.be/help/background/traprad/traprad.html.

[38]D. M. Sawyer and J. I. Vette, "Ap-8 trapped proton environment for solar maximum and solar minimum. [ap8max and ap8min]," (1976).

[39]M. Siegl, *Standard radiation environment monitor - simulation and inner belt flux anisotropy investigation [online]*, Master thesis, 2009.

[40]M. de Soria-Santacruz Pich, I. Jun, and R. Evans, "Empirical radiation belt models: comparison with in situ data and implications for environment definition," Space Weather **15**, 1165–1176 (2017).

[41]T. Tavenner, E. Fenimore, M. Galassi, R. Vanderspek, et al., "The Effectiveness of the HETE-2 Triggering Algorithm," in Gamma-ray burst and afterglow astronomy 2001: a workshop celebrating the first year of the hete mission, Vol. 662, edited by G. R. Ricker and R. K. Vanderspek, American Institute of Physics Conference Series (Apr. 2003), pp. 97–100.

[42]H. D. Thien Binh, *Job clustering: an unsupervised approach for a recommender system of skill requirements [online]*, Master thesis, SUPERVISOR : Dr. Peter H.G. Hendrix, 2021.

[43]VZLUSAT-2, [Accessed: 20.4.2024], (2024) https://www.vzlu.cz/snimky-planety-a-gama-zablesky-druzice-vzlusat-2-slavi-dva-roky-na-obezne-draze/.

[44]J. A. Van Allen, G. H. Ludwig, E. C. RAY, and C. E. McIlwain, "Observation of high intensity radiation by satellites 1958 alpha and gamma," Journal of Jet Propulsion **28**, 588–592 (1958).

[45]J. I. Vette, "The ae-8 trapped electron model environment," (1991).

[46]N. Werner, J. Řípa, A. Pál, M. Ohno, et al., "CAMELOT: Cubesats Applied for MEasuring and LOcalising Transients mission overview," in Space telescopes and instrumentation 2018: ultraviolet to gamma ray, Vol. 10699, edited by J.-W. A. den Herder, S. Nikzad, and K. Nakazawa, Society of Photo-Optical Instrumentation Engineers (SPIE) Conference Series (July 2018), 106992P.

[47]J. W. Wright, *Minimizing secular j2 perturbation effects on satellite formations [online]*, Master thesis, 2008.

[48]K. Yamaoka, M. Ohno, M. S. Tashiro, et al., Publications of the Astronomical Society of Japan **69**, R2 (2017).

[49]J. Řípa, G. Dilillo, R. Campana, and G. Galgoczi, "A comparison of trapped particle models in low earth orbit," in Space telescopes and instrumentation 2020: ultraviolet to gamma ray, edited by J.-W. A. den Herder, K. Nakazawa, and S. Nikzad (Dec. 2020).

[50]J. Řípa, A. Pál, M. Ohno, N. Werner, et al., "Early results from grbalpha and vzlusat-2," in Space telescopes and instrumentation 2022: ultraviolet to gamma ray, edited by J.-W. A. den Herder, K. Nakazawa, and S. Nikzad (Aug. 2022).